

THE GLOBULAR CLUSTER SYSTEM OF M87



STRUCTURAL PARAMETERS OF THE M87 GLOBULAR
CLUSTER SYSTEM

By

JUAN PABLO MADRID GAMBOA, M.Sc.

A Thesis

Submitted to the School of Graduate Studies
in Partial Fulfilment of the Requirements
for the Degree
Master of Science

McMaster University

©Copyright by Juan Madrid Gamboa, July 2009

MASTER OF SCIENCE (2009)
(Department of Physics and Astronomy)

McMaster University
Hamilton, Ontario

TITLE: Structural Parameters of the M87 Globular Cluster System

AUTHOR: Juan Madrid Gamboa, M.Sc.

SUPERVISOR: Prof. William E. Harris

NUMBER OF PAGES: x, 80

Abstract

We derive structural parameters for ~ 2000 globular clusters in the giant Virgo elliptical M87 using extremely deep Hubble Space Telescope images in F606W (V) and F814W (I) taken with the ACS/WFC. The cluster scale sizes (half-light radii r_h) and ellipticities are determined from PSF-convolved King-model profile fitting. We find that the r_h distribution closely resembles the inner Milky Way clusters, peaking at $r_h \simeq 2.5$ pc and with virtually no clusters more compact than $r_h \simeq 1$ pc. The metal-poor clusters average 24% larger in r_h than the metal-rich ones. The cluster scale size shows a gradual and noticeable increase with galactocentric distance. Clusters are very slightly larger in the bluer waveband V , a possible hint that we may be beginning to see the effects of mass segregation within the clusters. We derive a color magnitude diagram for the M87 globular cluster system which show a clear bimodal distribution. We analyzed in the detail the sub-structure of the CMD by applying statistical fits to the color distribution. We obtain a Globular Cluster Luminosity Function for all M87 clusters and for its red and blue subpopulations. The best statistical fits describing the Luminosity Functions were also calculated. The metal-poor subpopulation has a brighter peak (mean) than the metal-rich subpopulation.

Acknowledgements

My Parents are an unwavering and tremendous source of support for all the projects I decide to carry out, including this one. Laura Schwartz has been a source of happiness, motivation and positive attitude for me during the last four years of my life and without her help I would not have been able to move to Hamilton.

I would like to thank Prof. Bill Harris for sharing his expertise in globular clusters with me, for his time dedicated to this enterprise, and for always answering my questions. John Blakeslee and Matías Gómez were two outstanding collaborators in this venture. Hua Wu provided all the computer support to carry out this project.

Dean McLaughlin suggested McMaster University to do my graduate work.

I am indebted to my Astrophysics professors at McMaster: Christine Wilson, Alison Sills, Ralph Pudritz, Ethan Vishniac, James Wadsley, Doug Welch.

Discussions with Brad Whitmore, Paul Goodfrooij, and Iskren Georgiev (STScI) inspired me to write the “future prospects” section of this thesis.

During the last year I had two truly exceptional office mates: Charles-Philippe Lajoie and Nathan Leigh. My fellow students always provided a very cordial atmosphere and were always there when needed: Rachel Anderson, Rob Cockcroft, Jen Golding, Kristin Woodley, Yasuhiro Hasegawa, Philippe Boisvert, Chris Añorve, Victor Arora, Brendan Sinnott, David Kirsh.

I am grateful to the friendly staff of the Department of Physics and Astronomy for kindly sorting out a variety of administrative issues on my behalf: Mara Esposto, Cheryl Johnston, Rose McNeice, Liz Penney and Tina Stewart.

Phil Penner, my Yoga instructor at the McMaster Athletic Center, helped me to stay relaxed and breathing well while doing this work.

To my Parents, and to Laura

Table of Contents

Abstract	iii
Acknowledgements	iv
List of Figures	viii
List of Tables	x
Chapter 1 Introduction	1
1.1 Introduction	1
1.2 Characteristics of Globular Clusters	3
1.3 Thesis Objectives	5
Chapter 2 Observations and Data Reduction	8
2.1 Observations	8
2.2 Data Reduction	9
2.2.1 Multidrizzle	9
2.2.2 APSIS	10
2.2.3 Detection	11
2.3 PSF Modeling	12
Chapter 3 Comparison with a Recent Study: Waters et al. 2009	16
Chapter 4 Structural Parameters	18

4.1	Effective Radius	18
4.2	Concentration Parameter	23
4.3	Ellipticity	25
4.4	Position Angle	26
4.5	Effective Radius as a Function of Galactocentric Distance . . .	26
Chapter 5 Color-Magnitude Diagram		40
5.1	Photometry	40
5.2	Color-Magnitude Diagram	42
5.2.1	Bimodality	42
5.2.2	Comparison with the Waters et al. (2009) CMD	45
5.3	Statistical Fitting	45
5.4	Effective Radius versus Magnitude	49
Chapter 6 Globular Cluster Luminosity Function for M87		58
6.1	Globular Cluster Luminosity Function	58
6.2	Metal-poor and Metal-rich GCLF	61
Chapter 7 Summary and Future Prospects		67
Appendix A		77
Appendix B		79

List of Figures

1.1	Hubble Heritage image	7
2.1	Median subtracted image with detected clusters	13
4.1	ISHAPE profile fitting	19
4.2	Scatter in r_h	21
4.3	Cluster r_h in F606W vs. cluster r_h in F814W	29
4.4	Histogram of effective radius in F606W and F814W	30
4.5	Histogram of ratio of effective radius in F606W/F814W	31
4.6	Concentration Parameter	32
4.7	χ^2 for $c = 30, c = 100$	33
4.8	Ellipticity	34
4.9	Position Angle	35
4.10	r_h vs. galactocentric distance	36
4.11	Median value of r_h as a function of galactocentric distance	37
4.12	FWHM of sources with zero effective radius across the field	38
4.13	Number of globular clusters as a function of galactocentric distance	39
5.1	Curves of growth for synthetic sources	51
5.2	Flux correction as a function of cluster FWHM	52
5.3	Color-Magnitude Diagram	53

5.4	Histogram of globular cluster colors	54
5.5	RMIX fits to the CMD	55
5.6	RMIX fits to the “bridge” of intermediate metallicity clusters	56
5.7	r_h vs. magnitude for the two subpopulations of clusters	57
6.1	Globular Cluster Luminosity Function	63
6.2	Globular Cluster Luminosity Function and RMIX fits	64
6.3	GCLF of metal-poor clusters	65
6.4	GCLF of metal-rich clusters	66
7.1	Unidentified transient sources	71

List of Tables

5.1	Results of RMIX fits to the Color-Magnitude Diagram	47
6.1	Results of RMIX fits to the Globular Cluster Luminosity Function	62
7.1	Exposures with failed guide-stars	77
7.2	Position, effective radius, magnitudes	79

Chapter 1

Introduction

1.1 Introduction

Messier 87 (Virgo A, and NGC 4486) is the central dominant elliptical galaxy of the Virgo Cluster located 16.7 Megaparsecs away from us (Blakeslee et al. 2009). M87 is one of the most fascinating and best studied celestial objects and due to its relative close distance it has been a prime target of observations that have provided precious clues for the understanding of black hole physics, accretion disks, radio galaxies, and jets, among many other phenomena.

M87 has also played a crucial role in the understanding of extragalactic globular cluster systems (GCS). One of the most notable characteristics of this galaxy is its extremely large number of globular clusters. Recent ground-based observations found that the M87 GCS has in total more than 14000 members (Tamura et al. 2006a). The M87 GCS is also the paradigmatic high specific frequency (S_N) globular cluster system (McLaughlin et al. 1994, Harris 2009). The specific frequency represents the number of clusters per unit

galaxy luminosity (Harris & van den Bergh 1981) and for M87 $S_N=14$, a value three times higher than other Virgo giant ellipticals (McLaughlin et al. 1994, Peng et al. 2008). This large sample of globular clusters (GC) constitutes a superb statistical basis for carrying out many studies, including now accurate measurements of their structural parameters.

The large number of globular clusters belonging to M87 was first noticed in 1955 (Baum 1955) but the study of their structural parameters, e. g. characteristic sizes, ellipticities, luminosities, was enabled only by the superior angular resolution of the Hubble Space Telescope (HST). A typical size expected for a globular cluster, namely $r_{eff} \sim 2$ to 3 parsecs in radius, corresponds to only about $0.035''$ at the Virgo distance, or one pixel of the instruments onboard HST (Larsen et al. 2001). Previous work of this type for the globular clusters in the Virgo cluster members was done by Jordán et al. (2005, 2009) with ACS data but with much shorter-exposure data than we report here. Even earlier work for M87 (Kundu et al. 1999) used the WFPC2 with its larger pixel scale and smaller field of view, and is now superseded by the capabilities of the ACS. In fact, the ACS with its larger field of view and superb photometric accuracy has greatly contributed to the understanding of extragalactic globular cluster systems (Brodie & Strader 2006).

In this study we use one of the deepest datasets in the HST archive to derive the structural parameters for globular clusters in M87. A large, multi-orbit program imaging the central region of the galaxy was carried out with the Advanced Camera for Surveys and produced exceptionally deep images of the inner region of M87 (GO 10543, PI: Baltz), a region heavily illuminated

by galaxy light and difficult to image in such detail with a telescope of lower resolution or image quality. In this very deep dataset more than two thousand sources are globular clusters, and their radial profiles are distinctly and obviously larger than the PSF of the HST/ACS. We use the fact that these clusters are resolved to measure their structural parameters with ISHAPE, a software specially designed to derive these parameters for marginally resolved objects (Larsen 1999).

1.2 Characteristics of Globular Clusters

All clusters in M87 are halo or globular clusters given that there is no disk component in elliptical galaxies. Globular clusters are homogeneous stellar populations that are easy to observe at cosmic distances. Globular clusters are unique *and* accessible tracers of both the dynamical history and the star formation history of their host galaxies (e.g. Puzia et al. 1999). Studies of the spatial distribution of globular clusters with different metallicities in galactic halos have provided crucial input to theories explaining galaxy formation. Globular clusters are stellar tokens exchanged during mergers and thus privileged witnesses of galaxy interactions (West et al. 2004). Globular clusters are also correlated with star formation; evidence of this link is observed today in regions of active star formation such as M51 where a large number of clusters are presently forming (e.g. Lee et al. 2005). There is also a correlation between the number of clusters and the total stellar mass of the host galaxy (McLaughlin 1999). Globular clusters are thus “authentic guides to galaxies” (Richter & Larsen 2008).

Both internal and external factors give globular clusters their shape, colors, and masses. For instance, two-body relaxation and binary star fraction within the clusters influence their morphologies. Similarly, external factors such as the host galaxy tidal field also affect the characteristics of clusters. In the study of the morphologies of individual globular clusters a number of standard radii are commonly used: core radius (r_c), tidal radius (r_t), effective radius (r_h), half-light radius (r_{hl}), and half-mass radius (r_{hm}).

The core radius is the distance from the center of the cluster to where the surface brightness falls to half its central value. The tidal radius is the distance at which the surface brightness falls to 0, or where the dynamics of the individual stars are not dominated by the gravity of the cluster itself. The effective radius, or equivalently, the half-light radius, is the radius that contains half the total luminosity of the cluster. The effective radius is generally larger than the core radius. The half-mass radius r_{hm} is the radius that contains half the mass of the cluster. We should note that these radii can be defined both in three dimensions or in a projected two dimensional space. Observationally we are constrained to work in a projected 2D space.

One of the defining characteristics of clusters is a high stellar density in the central regions and a more sparse stellar distribution in their outskirts (Ashman & Zepf 1998). Thus, another important structural value is the concentration parameter c defined as the ratio of the tidal radius over the core radius $c = r_t/r_c$. This concentration parameter is usually quoted in relation to the models of globular clusters surface brightness profiles developed by King (1962,1966). The King models are based on an underlying dynamical repre-

resentation that treat globular clusters as collections of stars considered as point sources that interact through their gravitational attraction, exchanging energy during close encounters like gas molecules in random motion.

1.3 Thesis Objectives

The effective radius is an essential structural parameter which remains virtually constant through up to ten relaxation times and is an important and robust observable which constrains the understanding of evolutionary processes of globular clusters systems back nearly to the proto-cluster stage (Spitzer & Thuan 1972, Aarseth & Heggie 1998, Gómez et al. 2006). In this work we are able to precisely derive the effective radius of ~ 2000 clusters at an unprecedented signal to noise ratio. With HST the measurement of globular cluster effective radii in galaxies beyond the Milky Way and the Local Group became possible. The new ACS dataset we study here allow us to measure the effective radius of clusters and probe its dependence to galactocentric distance to up to 12 kpc away from the nucleus. We are also capable of estimating the effective radius as a function of color and luminosity for all clusters.

The M87 clusters are associated with the very dense environment of the Virgo Cluster core in a supergiant elliptical and thus their structural parameters give us the opportunity to probe a very different environment than the ones in the Milky Way. Through this work we are able to investigate the universality of the globular clusters morphology. It is indeed surprising that clusters, and globular cluster populations belonging to galaxies of completely different Hubble type, such as M87 and the Milky Way for instance, have strik-

ingly similar structural parameters, luminosity function and color distribution (Ashman & Zepf 1998). What are the properties innate to globular clusters and what are their characteristics related to their host galaxies?

This thesis is organized as follows: in Chapter 2 we describe the observations, data reduction, and PSF modeling we did for this project, in Chapter 3 we compare this work with a recent study using the same dataset, in Chapter 4 we present our results related to the structural parameters of the M87 globular clusters, in Chapter 5 we analyze the color-magnitude diagram while in Chapter 6 we give the globular cluster luminosity function, and in Chapter 7 we summarize the main findings of this work.

We use throughout this work $H_0=71 \text{ km.s}^{-1}\text{Mpc}^{-1}$, $\Omega_M = 0.27$, and $\Omega_\Lambda = 0.73$. At the distance of M87, $1''$ corresponds to 80 pc (Wright 2006).

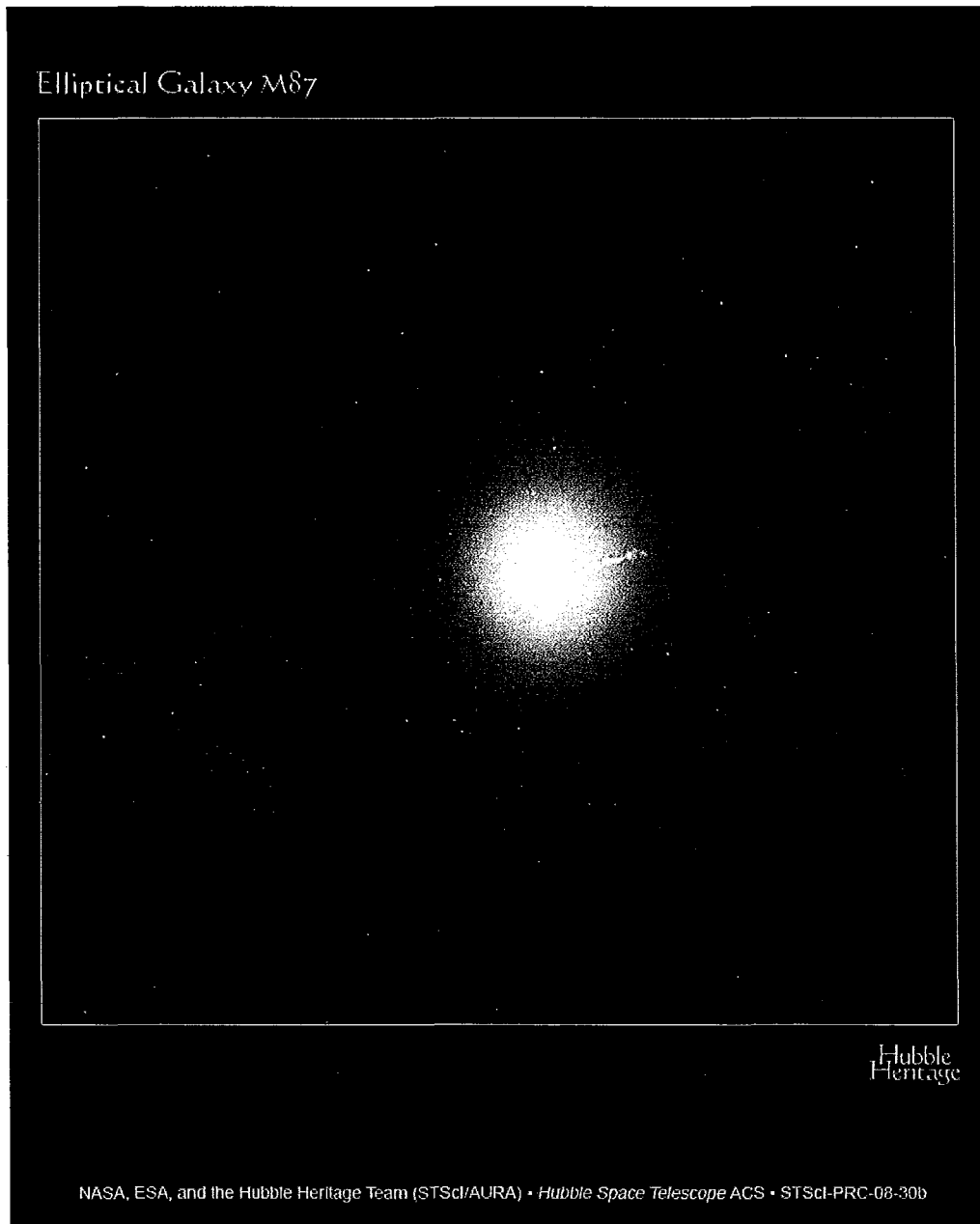


Figure 1.1 Hubble Heritage image created by the STScI Heritage Team at our insistence and with our collaboration. This image was built with the data we use in this thesis and supplemental color data (F475W) obtained during the ACS Virgo Cluster Survey by Pat Côté and collaborators.

Chapter 2

Observations and Data Reduction

2.1 Observations

Our images were taken with the ACS Wide Field Channel (WFC), which has a $202'' \times 202''$ field of view and a pixel scale of $0.05''$ (Mack et al. 2003, Gonzaga et al. 2005). The ACS observations that we analyze were taken in two filters: F606W (wide V) and F814W (equivalent to I). The original program of these observations was aimed at finding microlensing events towards M87. These microlensing events are expected to be red (Baltz et al. 2004) and therefore the observations were heavily weighted to F814W, with 205 images and a total of 73800 seconds. The F606W observations were intended to provide supplementary color information, and comprise 49 images totaling 24500 seconds. The data was taken over a period of 71 days, from 2005 Dec 24 to 2006 Mar 05 in 61 different visits. These observations were obtained following a dither pattern that allows sub-pixel drizzling.

2.2 Data Reduction

We retrieved the flatfielded science files `FLT.FITS` from the Multimission Archive at Space Telescope (MAST). These files were prepared through the standard “on the fly reprocessing” (OTFR). The OTFR system processes the raw HST data using up-to-date software and calibration files. For the Advanced Camera for Surveys the automatic reduction and calibration pipeline (`CALACS`) performs bias subtraction, dark current subtraction, and flatfielding before delivery of each `FLT.FITS` file (Sirianni et al. 2005).

The number of images and exposure times given in the section above correspond to those exposures with correct pointings. In fact, several exposures in HST GO program 10543 contain blank fields or random pointings due to a failure in guide-star acquisition. After retrieving the data from the archive the first task was to “weed out” these failed exposures which are documented in detail in Appendix A.

2.2.1 Multidrizzle

`MULTIDRIZZLE` is the standard software distributed by the STScI for image combination of ACS data. While `MULTIDRIZZLE` is very effective in combining single-orbit data, it requires the additional input of residual shifts for exposures taken during multi-orbit programs as described below. All our exposures have the same orientation, i.e. the same PA-V3, which allows `MULTIDRIZZLE` to register the images correctly to a first order. `MULTIDRIZZLE` uses the World Coordinates System (WCS) in the image header for registration. When the data to be combined is taken during different visits using different guide stars

the WCS information is not accurate enough to ensure proper registration. Residual shifts of individual exposures must be calculated and provided to MULTIDRIZZLE. In our case these residual shifts range from a thousandth of a pixel to five pixels. These residual shifts were obtained by identifying a large number of sources, generally about 1000 clusters, with the IRAF task DAOFIND and subsequently calculating the shifts from a reference image with GEOMAP. We calculated the residual shifts for all our images several times following the instructions provided by the STScI help desk but these shifts failed to converge causing residual misregistrations in our final image. We were thus constrained to use APSIS, an alternative software for image combination that we describe in the next section.

2.2.2 APSIS

Final combination of the images was done with the ACS Pipeline Science Investigation Software (APGIS). We use APSIS to do distortion correction, image registration, image combination, cosmic ray rejection, and drizzling (Blakeslee et al. 2003). APSIS was developed by the ACS science team and proved to be more effective than MULTIDRIZZLE at registering this large data set taken during different epochs. Using Python, APSIS performs subpixel drizzling. Drizzling is highly recommended for HST images which are affected by undersampling, namely, the pixel width is equal or larger than the PSF FWHM. Fruchter & Hook (2002) estimate that a well sampled detector should have 2.5 pixel across the PSF FWHM. As stated in the observations section above, this dataset was taken following a dither pattern that allows subpixel

drizzling. In other words, the positions of different exposures are offset by a few non-integer pixels to better sample the PSF. The final drizzled image has higher resolution than the individual exposures, we chose to construct the final science images with a pixel scale of $0.035''/\text{pixel}$. We use a Gaussian function as interpolation kernel and a pixel fraction (`pixfrac`) of 1.

As a test of the reliability of our results, all measurements described below were also performed on an image with a narrower PSF. An image with a 10% narrower PSF was built by using a smaller value for `pixfrac` (0.5 instead of 1.0) during the data reduction. The final cluster sizes measured from these two different reductions were identical. Using a different fitting code (`KINGPHOT`), Peng et al. (2009) come to the same conclusion that we do here, the differences between magnitudes and sizes are negligible between the two reductions.

2.2.3 Detection

From the master combined F606W and F814W images we created a median subtracted image to eliminate the galaxy light in order to facilitate the detection of the position of globular clusters on our images. The `pyraf` task `DAOFIND` did a better job than `SExtractor` detecting point sources and ignoring brightness fluctuations and background galaxies. We performed a careful visual inspection of the frame to verify these detections. We manually removed spurious sources along the edges of the different knots belonging to the prominent M87 jet. Large gradients in brightness are often misinterpreted as sources by `DAOFIND`. We also removed spurious detections along the edges of the image. We detect a total of 2010 objects on our images almost all of

which are globular clusters. In Figure 2.1 we show a section of the median subtracted image with our detections of cluster candidates. Given the very large number of clusters in our sample a few field contaminants should have a negligible impact on our results (Larsen et al. 2001). We should note that we performed all measurements presented below on the original images, the median subtracted image was used only to locate the clusters. Systematics introduced by a routine such as MEDIAN or ELLIPSE are difficult to evaluate and therefore difficult to correct.

2.3 PSF Modeling

An accurate PSF is crucial for our purpose of deriving precise structural parameters for the GCs, given that we are working in a regime where the GC intrinsic sizes r_h are similar to the FWHM of the PSF itself. In principle, PSFs can be constructed through modeling techniques such as TinyTim, but extensive discussions of this approach in recent papers directed towards the same goal of measuring GC sizes in relatively nearby galaxies imaged with ACS (Spitler et al. 2006, Georgiev et al. 2008) show considerable difficulty matching the models to empirical PSFs derived directly from stars on the images. Working from this experience, we have adopted the approach of using purely empirical PSFs built from stars on the master F814W and F606W images described above.

An immediate practical issue is to find candidate stars on these images: of the more than 2000 detected objects on the field, roughly 98% are globular clusters belonging to M87 and these must all be weeded out. Fortunately, the

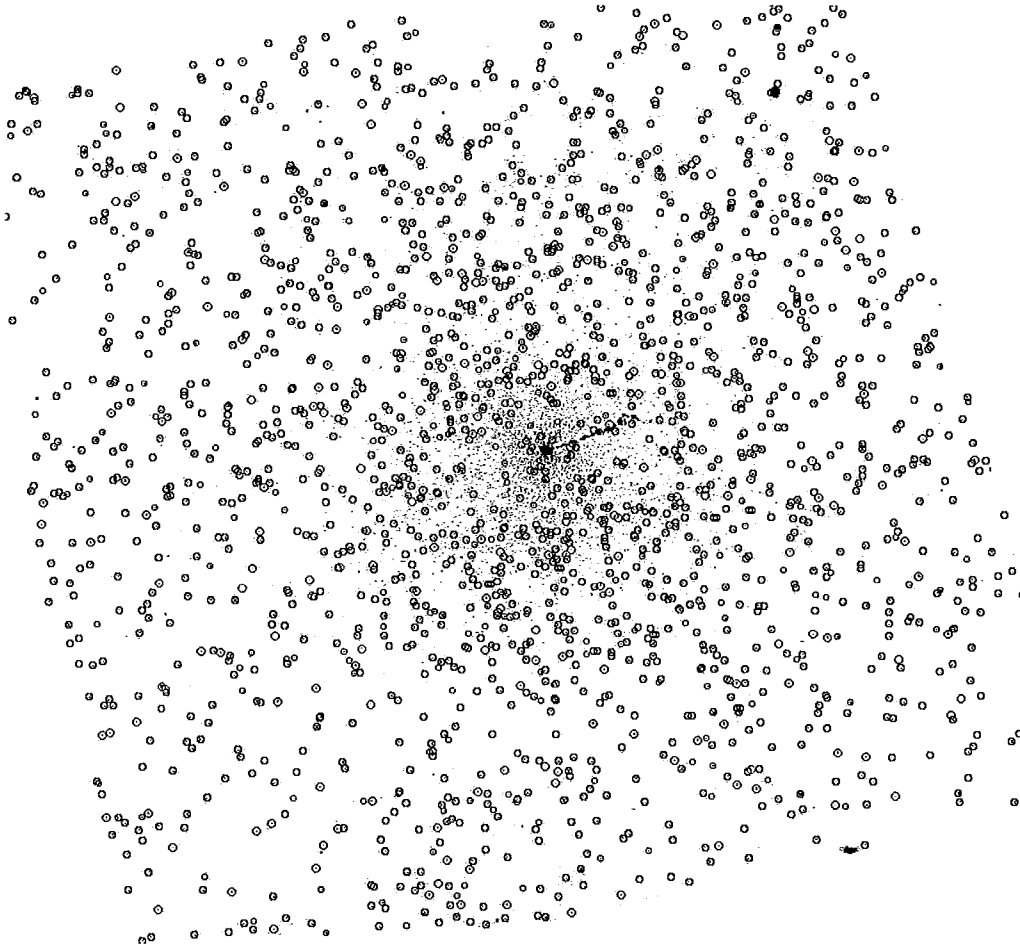


Figure 2.1 Median subtracted image of the ACS/WFC field of view of the inner region of M87. Detected clusters are shown by circles, the prominent plasma jet emanating from the super-massive black hole at the core of the galaxy is clearly visible. North is up and east is left.

true size of the stars is accurately known beforehand: for properly co-added images, the HST image resolution is $\simeq 0.095''$, and thus we expect genuine stars to have FWHM $\simeq 2.7 - 2.8$ pixels at our final drizzled scale of $0.035''/\text{px}$. Equally important for our purposes, as will be seen below, there is almost no overlap between the stars and the measured sizes of the GCs (that is, their intrinsic sizes convolved with the PSF), with a clear gap between the true stars and the smallest GCs.

To pick out the stars, we used the SExtractor software (Bertin & Arnouts 1996) to make preliminary measurements of the half-light radii and FWHMs of all 2000+ objects on our detection list, including GCs, stars, and a few small background galaxies. These scale sizes were plotted against the SE total aperture magnitude. On these diagnostic graphs, the stars then show up as an easily identified, narrow (though thinly populated) sequence clearly separated from the GCs and other objects. See, for example, Figure 2 of Harris (2009) for the same approach. We selected the 30 brightest of these and inspected them individually on the images, rejecting any with faint companions, nearby bad pixels, or other anomalies; one bright star that was at or near saturation was also rejected. Our final star list had 17 stars distributed uniformly across the ACS field, from which the PSF was then constructed. To minimize any later concerns about systematic differences between the F606W and F814W images in the measured GC parameters, we used exactly the same 17 stars to derive the PSF separately in each filter. The final PSF profiles have FWHMs of 2.75 pixels (F606W) and 2.78 pixels (F814W). We should note that, as a test to the solidity of our results, all measurements described below were also performed on an image with a narrower PSF. An image with a 10% narrower PSF can be

built by using a smaller value for `pixfrac` (0.5 instead of 1.0) during the data reduction. The final cluster sizes measured from these different reductions were identical.

We create the PSF for each filter by using the standard DAOPHOT routines within PYRAF. We perform photometry of the candidate stars with PHOT and then run PSTSELECT to select the stars to be used to build the PSF by the task PSF. The output of PSF is a luminosity weighted PSF with a radius of 79 pixels. We ensured that all stars used to calculate the PSF had similar luminosity and thus we avoid any bias in favor of particularly bright stars. We use SEEPSF to oversample our PSF to the pixel size required by ISHAPE, i.e. ten times smaller than the image pixel size (Larsen 1999).

Chapter 3

Comparison with a Recent Study:

Waters et al. 2009

A recent paper by Waters et al. (2009) analyzed the same dataset used here but aimed at discussing the mass/metallicity relation in the GCS and its color bimodality. Waters et al. (2009) do not make specific conclusions on structural parameters for the clusters themselves. We note below several steps in our analysis of this dataset that differ from their work.

A first important difference in our data reduction concerns the final combined image that we use to measure the structural parameters. In this study the final image is subsampled to a pixel scale of $0.035''$ taking thus full advantage of the dithered raw observations. Waters et al. (2009) keep the ACS camera native pixel size of $0.05''$. The PSF is also computed in a different fashion: Waters et al. (2009) use the software of Anderson & King (2006) while in this work we create a purely empirical PSF using a sequence of tasks described in the previous section.

The magnitudes and radii of ~ 2000 clusters, each with different size cannot be measured with either standard PSF-fitting or fixed aperture techniques. In

order to derive proper magnitudes both our work and Waters et al. (2009) compute flux corrections based on the size of each object. In this study we calculate the magnitudes by scaling the flux that we measure at a 5 pixel radius to large radius (30 px) using the curve of growth of each object appropriate to its particular effective radius. The details of this method are given in the photometry section. Waters et al. (2009) instead use the magnitude difference between a radius of 4 pixels and a radius of 2 pixels as the main parameter to estimate the cluster size and their aperture correction. Lastly, our measurement of cluster size is done with a different code, ISHAPE, and using a fiducial King-model concentration $r_t/r_c = 30$ that is more representative of the true mean for globular clusters than their adopted ratio of $r_t/r_c = 10$ (see section 5 below).

When compared with Waters et al. (2009) some of our methods are obvious improvements, such as obtaining an image with higher resolution, while other differences are an independent approach to measure the same quantity, such as the use of an alternate fitting profile code.

Chapter 4

Structural Parameters

4.1 Effective Radius

We use the software ISHAPE developed by Søren Larsen to calculate the effective radius, ellipticity, and position angle θ for each individual cluster on our images. In a detailed analysis of the properties of ISHAPE Harris (2009) finds that this code can recover the size and shape for clusters with $FWHM > 0.1FWHM(PSF)$. ISHAPE convolves an analytical model of the cluster profile with the PSF and finds the best fit to the data by performing iterative adjustments to the cluster profile FWHM. The analytical model used to fit the clusters is chosen by the user from a predefined list e. g. Gaussian, King, Sersic, see Larsen (1999). We use model King profiles (King, 1962) with a concentration parameter of $c=30$, where $c = \frac{r_t}{r_c}$, the ratio of the tidal radius divided by the core radius:

$$f(r) = \left\{ \frac{1}{\sqrt{1+(r/r_c)^2}} - \frac{1}{\sqrt{1+(r_t/r_c)^2}} \right\}^{1/2}$$

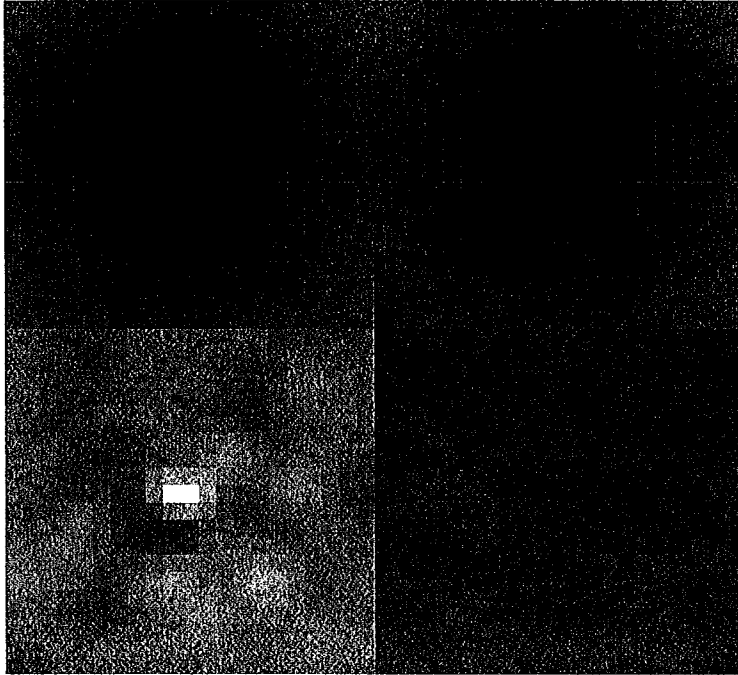


Figure 4.1 Example illustrating the ISHAPE profile fitting procedure. One observed M87 cluster is on the upper right and the best model convolved with the PSF is on the upper left. The lower left image is the residual image resulting from the subtraction of the model from the observed cluster. The lower right quadrant is the weight map.

The value $c = 30$ accurately represents the average of real globular clusters (Harris 1996, Larsen 1999, Larsen et al. 2001). By contrast, Waters et al. (2009) used $c=10$, a value near the *minimum* for real globular clusters rather than the mean.

The measurement of the effective radius carried out by ISHAPE is robust and nearly independent of the fitting function. We set a fitting radius of six pixels and we convert our measurements of the cluster FWHM into the effective radius by following the prescription of Larsen (1999). Namely, we convert the

ISHAPE internal radius, which is model dependent, into a model independent quantity $r_h = 1.48 \times FWHM$, where 1.48 is the appropriate factor for $c=30$. We obtain thus the cluster size in pixels, we multiply by the scale, and then obtain the cluster r_h in arcseconds. All clusters considered in the following analysis have an effective radius measured with a signal-to-noise ratio > 50 . This high-quality requirement for the results generated by ISHAPE brings the number of clusters from 2010 raw detections to 1981 clusters in F814W and 1907 clusters in F606W with reliable estimates of their structural parameters. Results are shown in Figures 4.3 and 4.4.

Strictly, ISHAPE measures the r_h along the major axis of the profile and in theory a small correction should be made to derive r_h for a non-circular cluster (Larsen 2008). Given that most clusters of our sample are nearly circular we quote the direct values of r_h given by ISHAPE without further corrections for the effects of the ellipticity during the fitting process. Details on the sensitivity of our measurements to cluster ellipticity and a test to the validity of our assumptions is given in Harris (2009).

An extensive set of tests and simulations to characterize the uncertainties associated with ISHAPE measurements is presented in Harris (2009). In this work it is clearly shown that ISHAPE derives accurate values for cluster effective radius, ellipticity and position angle when $S/N > 50$, this is precisely the cut-off that we adopt in this study. The main sources of error in the size measurements can be summarized in three components: the ISHAPE fitting procedure itself, the uncertainty in the true values of the concentration parameter c , and the error associated with the estimate of the size of the PSF. The random

uncertainty per object taking into account the three sources of uncertainty cited above is $\sigma_{r_h} = \pm 0.006''$ (Harris 2009) for his BCG data sample. For comparison, the rms scatter around the 1:1 line in Figure 4.3 is $\pm 0.004''$; this value should give a reasonable estimate of our internal measurement uncertainty since it is the direct comparison of two independent measurements of the same objects in different filters. The equivalent uncertainty for r_h is then ± 0.3 pc as illustrated in Figure 4.2 below.

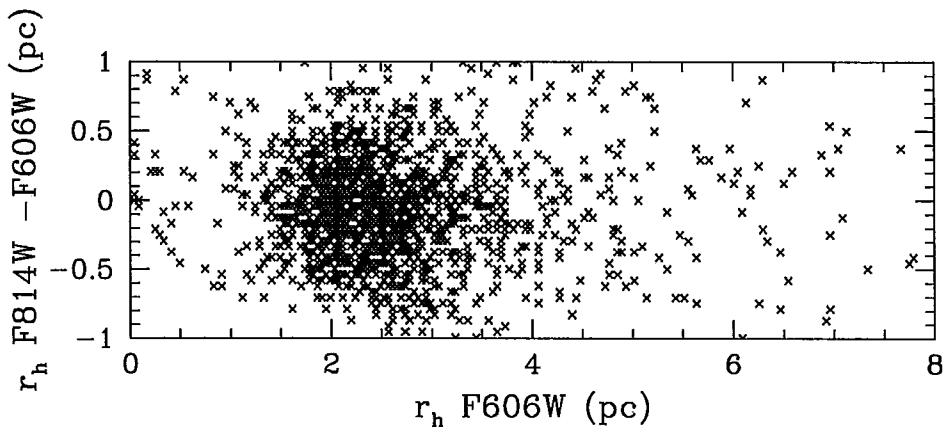


Figure 4.2 Scatter in r_h measurements in two bands.

The values for the linear effective radii that we derived are in good agreement with the values of Milky Way globular clusters. The Milky Way has 142 clusters with known effective radius, out of these 142 clusters 114 (80%) have an effective radius between 1 and 6 pc (Harris 1996). It can be seen in Figure 4.3 and the histogram in Figure 4.4 that most M87 clusters also have an effective radius between 1 and 6 parsecs and peak at very much the same radius ($\simeq 2.5$ pc) as the Milky Way.

We recover the well documented size difference between red (metal-rich) and blue (metal-poor) clusters, i.e. blue clusters are 24% larger than red ones in the M87 GCS (a result first noted by Kundu et al. 1998), as discussed further below.

It is intriguing that clusters belonging to two galaxies with different Hubble type have the same size distribution. Forbes (2002) plotted side by side the size distribution of GCS for five galaxies of completely different Hubble type: cD, gE, S0, Sa, Sbc. Strikingly, the size distribution of the overall GCS and of both subpopulations are very similar. The physical processes determining the size of globular clusters and the size difference between the two sub-populations are independent of galaxy type. Whitmore et al. (2007) suggest a universal initial mass function for clusters followed by an evolution dominated by internal dynamics. The host galaxy has only a secondary effect on cluster size.

We also find a hint of a size difference with respect to wavelength such that the cluster size measured in $F606W$ is very slightly larger on average than in the $F814W$. For all clusters we calculated the ratio $\frac{r_h^{F606W}}{r_h^{F814W}}$; the histogram of the values of this ratio is plotted in Figure 4.5. Of the 1896 clusters which are within our high confidence range 61% of them have $r_h^{F606W} \geq r_h^{F814W}$. The median ratio, near the peak of the histogram, is 1.02 ± 0.006 and the standard deviation is 0.24. We rejected objects at more than 3σ level as outliers. We are well aware that the mean difference may have arisen from small residual systematics although we have attempted to minimize any such systematics as much as possible, and we should note that the very small raw difference between the two PSF sizes noted above is not large enough by itself

to produce the difference we see, particularly for bigger clusters. However, if the difference in mean r_h between the two filters is physically real, we suggest that we may be seeing the visible results of *mass segregation*. Dynamical evolution of the population of stars within each cluster drives the less massive stars to larger radii and the more massive ones inward toward the core, while maintaining a nearly constant r_h . Over time, a secondary observational effect is that the cluster effective radius will look progressively smaller in redder bandpasses that systematically favor the light from the massive red-giant and subgiant stars, compared with the bluer, lighter upper-main-sequence stars that preferentially populate the outskirts. To gauge the expected size of the effect, we have used the predicted r_h values in the B, V, I bandpasses for model globular clusters with an initial mass of $10^5 M_\odot$ evolved through an advanced N-body code (Hurley 2009, private communication; see also Hurley et al. 2008). After 10-12 Gy of dynamical evolution, the model clusters have measured r_h values that are 5% larger in V than in I . Both the direction and size of the effect are very close to the mean offset that we see in the M87 system. We view our result as only suggestive, but it may point the way to a valuable new test of our understanding of GC dynamical evolution.

4.2 Concentration Parameter

The concentration parameter for a globular cluster is defined as the ratio of the tidal radius over the core radius $c = r_t/r_c$. Dynamical evolution of star clusters drives the outer regions of clusters to expand and at the same time increases the central stellar density. The observable manifestation of the

rise in stellar density in the core is the presence of central *cusps* in surface brightness profiles and an increase in the concentration parameter (Djorgovski & Meylan 1993, de Marchi et al. 2007). The concentration parameter has been traditionally considered, at least partly, a tracer of the evolutionary state of globular clusters.

ISHAPE offers the possibility to set c as a free parameter and determine its value for each individual cluster during the fitting process. Using this ISHAPE option we ran a test aimed at precisely establishing the value of the concentration parameter. However, we were not able to draw any conclusion from this test: reasonable values for c are only determined in a few cases and do not show any particular trend with either magnitude or size. As noted by Gomez & Woodley (2007) the concentration parameter is the most uncertain of the fitted parameters.

Given that we set, based on *a priori* information, the concentration parameter at $c = 30$ we investigate the impact of a different value of c on the final effective radius. We ran two trials of ISHAPE with c set at 15 and 100. In Figure 4.6 the results of these two trials are compared with the results obtained running ISHAPE with $c = 30$. Figure 4.6 shows that for clusters with $r_h < 4pc$, the size of most clusters studied here, the effective radius is insensitive to the choice of c . However, for bigger clusters the choice of concentration parameter has a much greater impact on the effective radius derived by ISHAPE.

ISHAPE computes the best fitted structural parameters by minimizing a χ^2 function for each cluster (Larsen 2008). The value of the final χ^2 function is also an output of ISHAPE. We analyzed the values of χ^2 for the three different

runs with c values of 15, 30, and 100. We find that when χ^2 is small, i.e. < 50 , the best fit is neither improved nor degraded by the choice of c . When χ^2 is > 50 the best fit has a stronger dispersion, as shown in Figure 4.7.

After running these different tests on the concentration parameter we conclude that a cluster with effective radius of less than 4 pc and a small χ^2 (therefore with a good fit) can be well modelled with any value of c . Direct measurement of c for individual clusters in this dataset remains a challenge, however. As expected for our measurements, χ^2 is not correlated with the signal to noise ratio. The signal to noise ratio is sufficiently high for all clusters to obtain good fits to the data.

4.3 Ellipticity

We should note that while ISHAPE provides a fast and reliable measurement of the effective radius, results for more refined structural parameters such as ellipticity and position angle are less precise (Harris 2009). ISHAPE measures the ratio of minor/major axis and thus the ellipticity of each cluster. In Figure 4.8 we plot the values obtained with ISHAPE for the ratio of minor/major axis for 1767 clusters of our dataset. Similarly to the Milky Way globular clusters (Harris 1996) most M87 clusters are roughly spherical, i.e. for more than 55% of clusters in our sample the ratio minor/major > 0.8 . A normal two sample Kolmogorov-Smirnov test shows that the M87 and Milky Way distributions are formally different at high statistical significance. However, these two samples were measured in completely different ways: the Milky Way clusters are orders of magnitude better resolved and thus their ellipticities are

much better determined and physically meaningful. Figure 4.8 shows that, roughly, M87 clusters have the expected range of small ellipticity.

4.4 Position Angle

With ISHAPE we also obtain the position angle (PA) for each individual cluster. In Figure 4.9 we summarize the values taken by the PA of all clusters and for high-ellipticity clusters ($e > 0.2$). Neither the whole sample nor the subsample of high-ellipticity clusters exhibit an observable trend in PA values. We expect the M87 clusters to have a random orientation on the sky and thus the ensemble of PA values should be free of any trends or particular orientation.

4.5 Effective Radius as a Function of Galactocentric Distance

Hodge (1960, 1962) measured the sizes of Large Magellanic Cloud globular clusters using data taken with the ADH Baker-Schmidt telescope in South Africa. Despite the fact that Hodge (1962) observed a projected distribution instead of the real spatial distribution, he first recognized the correlation between cluster size and galactocentric radius (R_{gc}), i. e. cluster size increases with increasing distance to the center of the galaxy. Hodge (1962) postulated the tidal effects of the parent galaxy on the cluster as the most probable explanation for this effect. Based on data for Milky Way globular clusters, and therefore free of projection bias, van den Bergh et al. (1991) find a relation between cluster effective radius and true 3D galactocentric distance of

$r_h \propto \sqrt{R_{gc}}$. The same dependence of cluster size and galactocentric distance has been well documented in NGC5128 (Hesser et al. 1984, Gómez & Woodley 2007), NGC4594 (Spitler et al. 2006) and in six other giant ellipticals (Harris 2009). For these galaxies the general trend is for r_h to increase roughly as $r_h \sim R_{gc}^{0.1-0.2}$ where R_{gc} is the projected distance.

In Figure 4.10 we plot the effective radius r_h versus projected galactocentric distance R_{gc} . Our observations target the central regions of M87 where tidal forces exerted by the galaxy are expected to have the strongest effect limiting the size of clusters (Hesser et al 1984). For $R_{gc} \leq 5$ kpc the mean cluster size is nearly constant, but then begins to increase gradually, out to the limits of our data at $R_{gc} = 10$ kpc. In Figure 4.11 we plot the median effective radius for clusters versus galactocentric distance. The increase of cluster size with distance to the nucleus is evident. Kundu et al. (1999) failed to observe this trend most likely as a result of their smaller WFPC2 field size.

In order to demonstrate that the increase in effective radii of clusters with R_{gc} is real, we performed a test with the stars on the field. We selected all the objects that ISHAPE returned as having FWHM=0, that is the ones that are by definition starlike. There were 42 such stars; we then measured with IMEXAMINE the FWHM of these point sources. These stars can also be clearly seen in Figures 4.3, 4.4, & 4.10 as the sources around the zero value for the effective radius, and are also apparent in Figure 4.4 as the first bin of the histogram i.e. $r_h = 0$. We find that the FWHM of these point sources is consistent with the value of the PSF FWHM of 2.7 pixels, and more importantly does not show a dependence with galactocentric radius (see Figure

4.12). We also plot in Figure 4.12 (bottom panel) the residual of the PSF with unresolved sources across the detector. This additional test to the accuracy of the PSF shows that the residuals are minor and do not show any specific trend across the detector.

We plot the number of detected globular clusters as a function of galactocentric distance in Figure 4.13. Our sample is limited by the size of the ACS/WFC field of view that extends up to ~ 11 kpc in radius from the nucleus. A natural next step in this work is to extend the field coverage further away from the galactic center and study the evolution of r_h out to 50-70 kpc, this would be an interesting probe of the tidal field of the galaxy. A cycle 17 HST proposal was submitted aimed at pursuing this goal.

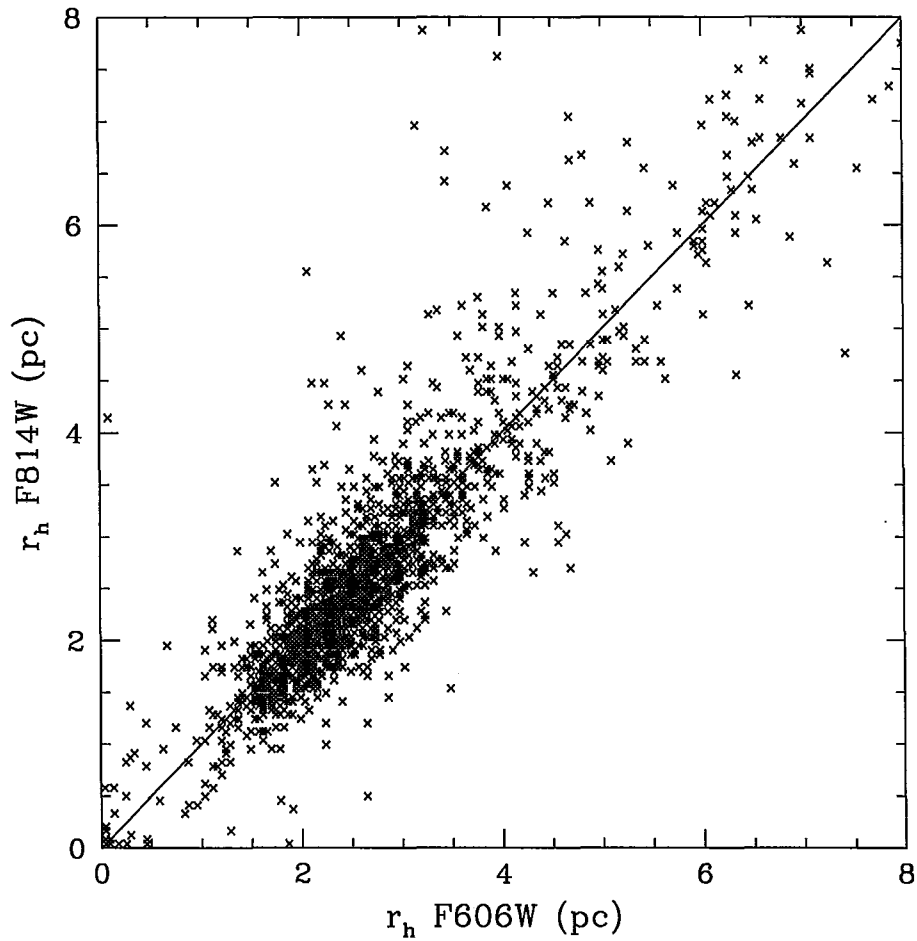


Figure 4.3 Cluster effective radius in F606W vs. cluster effective radius in F814W. Note the gap between a small number of unresolved clusters, clustering around 0, and the large majority of resolved clusters grouped around ~ 2.5 pc. The units of this graph are parsecs.

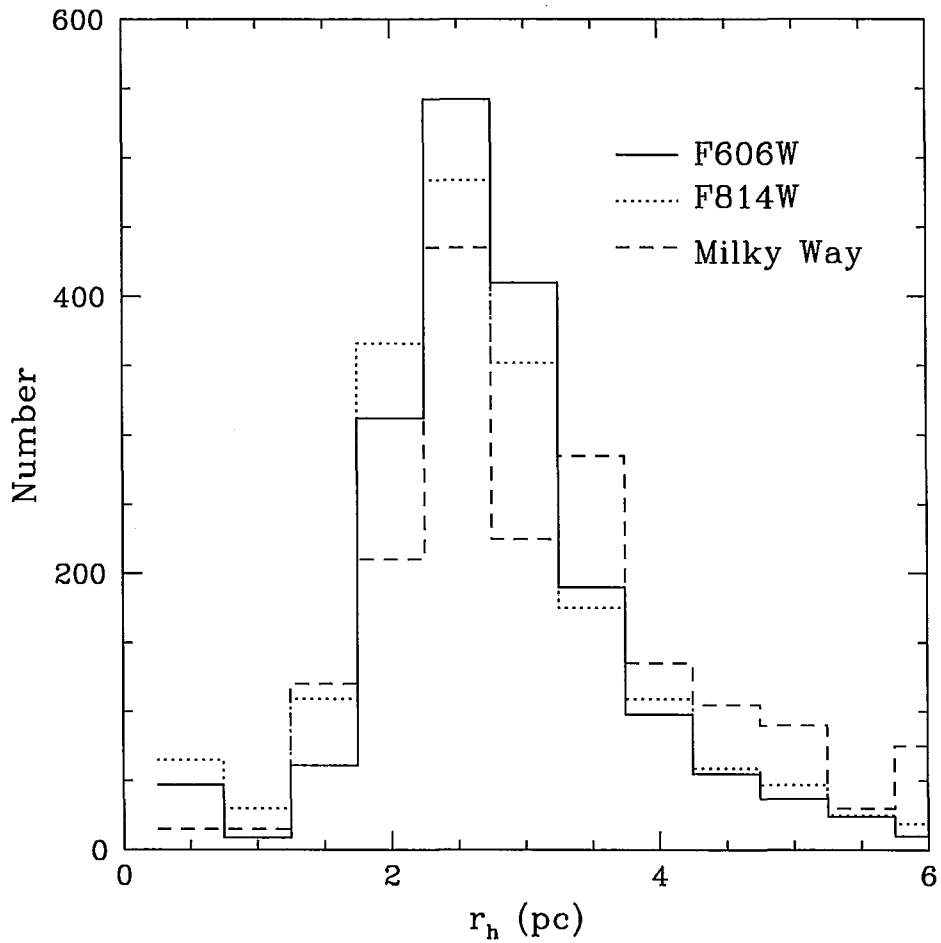


Figure 4.4 Histogram of effective radius in F606W and F814W. It can be seen on this figure how the effective radius of most clusters lies between 1 and 6 pc. The histogram of the effective radius for Milky Way clusters ($\times 15$) is overplotted for comparison.

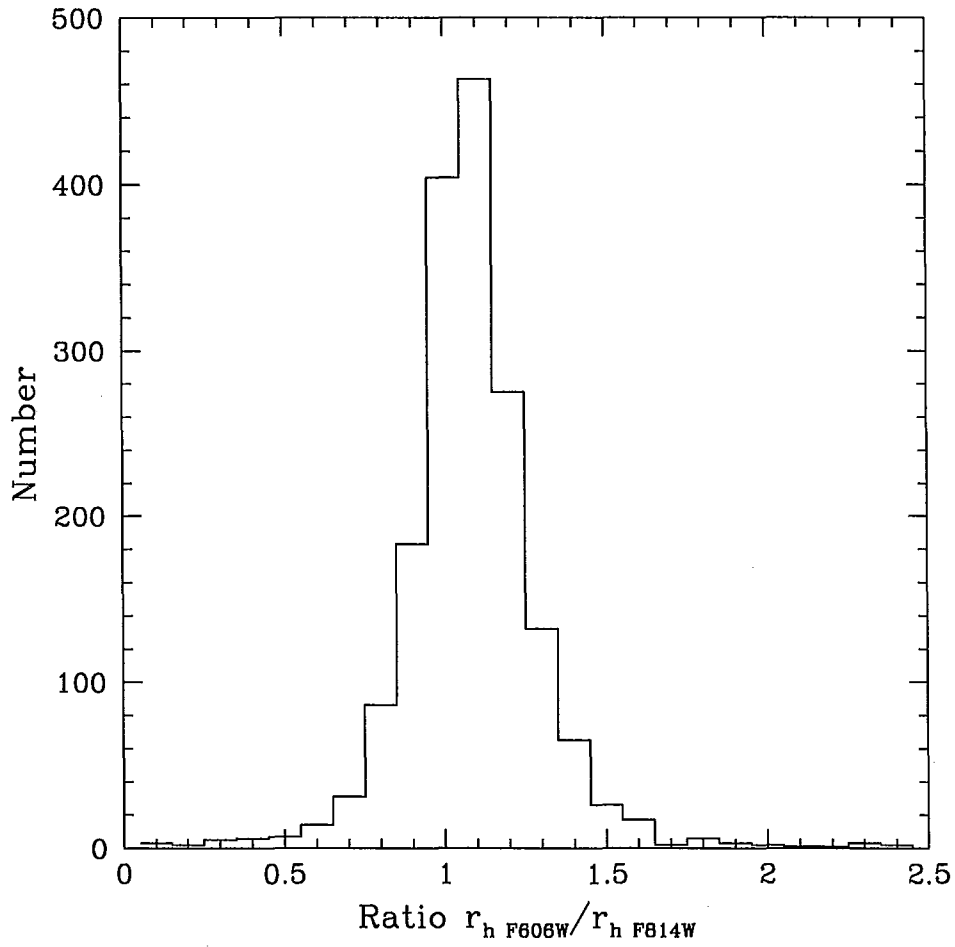


Figure 4.5 Ratio of the effective radius of M87 clusters in F606W over F814W, the median of this distribution is 1.02 with a standard deviation of 0.24.

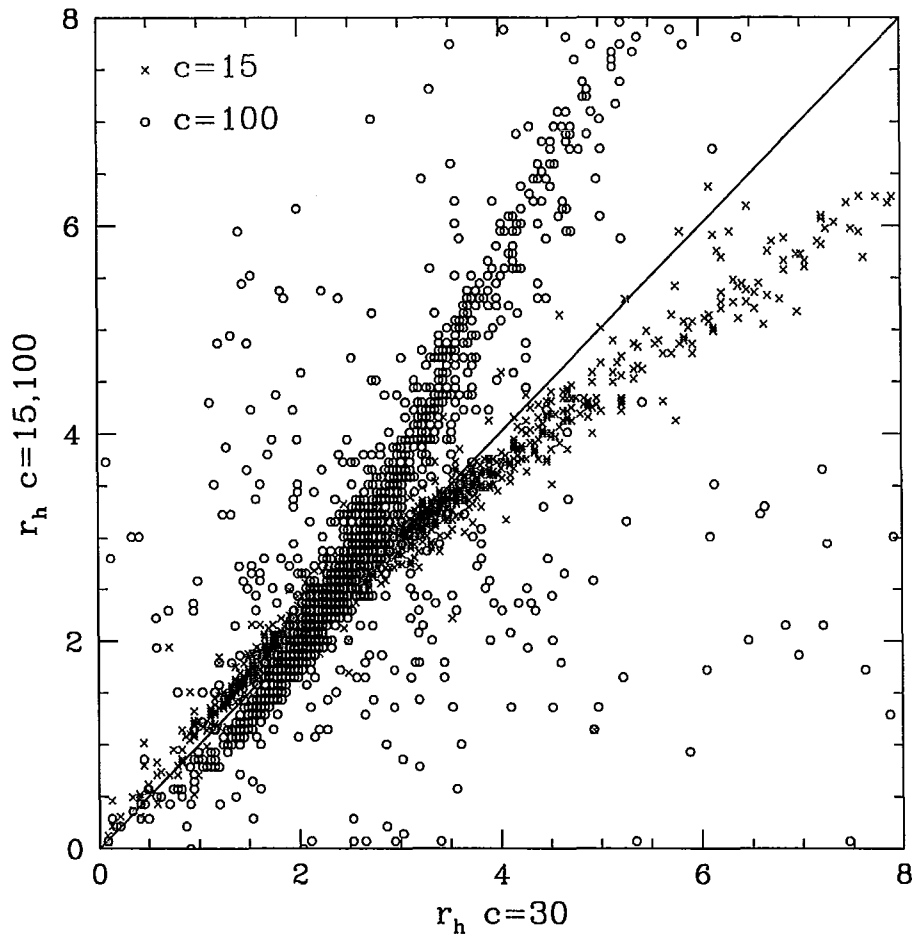


Figure 4.6 Comparison of r_h estimates using three different values for the concentration parameter $c = 15, 30, 100$. This comparison shows that the choice of c has a greater impact for clusters with larger r_h than for smaller clusters. The units of this graph are parsecs.

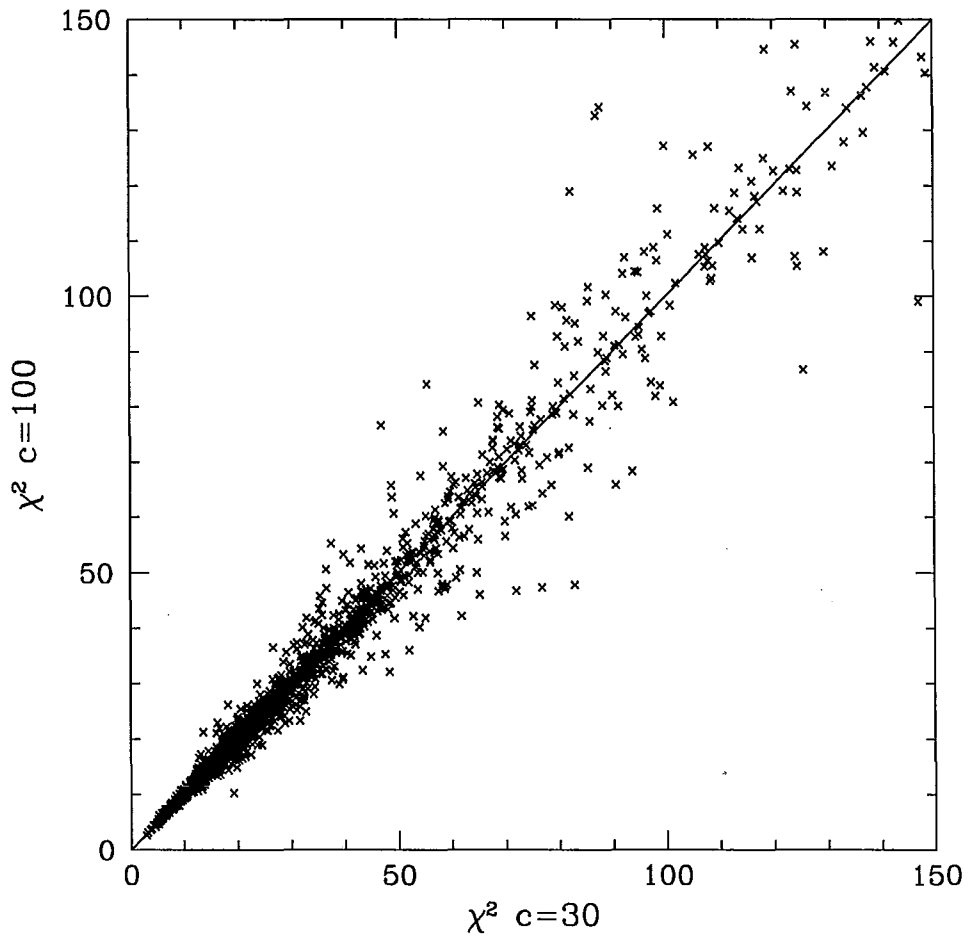


Figure 4.7 χ^2 values for two runs of ISHAPE with $c = 30$ and $c = 100$. The goodness of fit is identical in both runs for those clusters with small χ^2 .

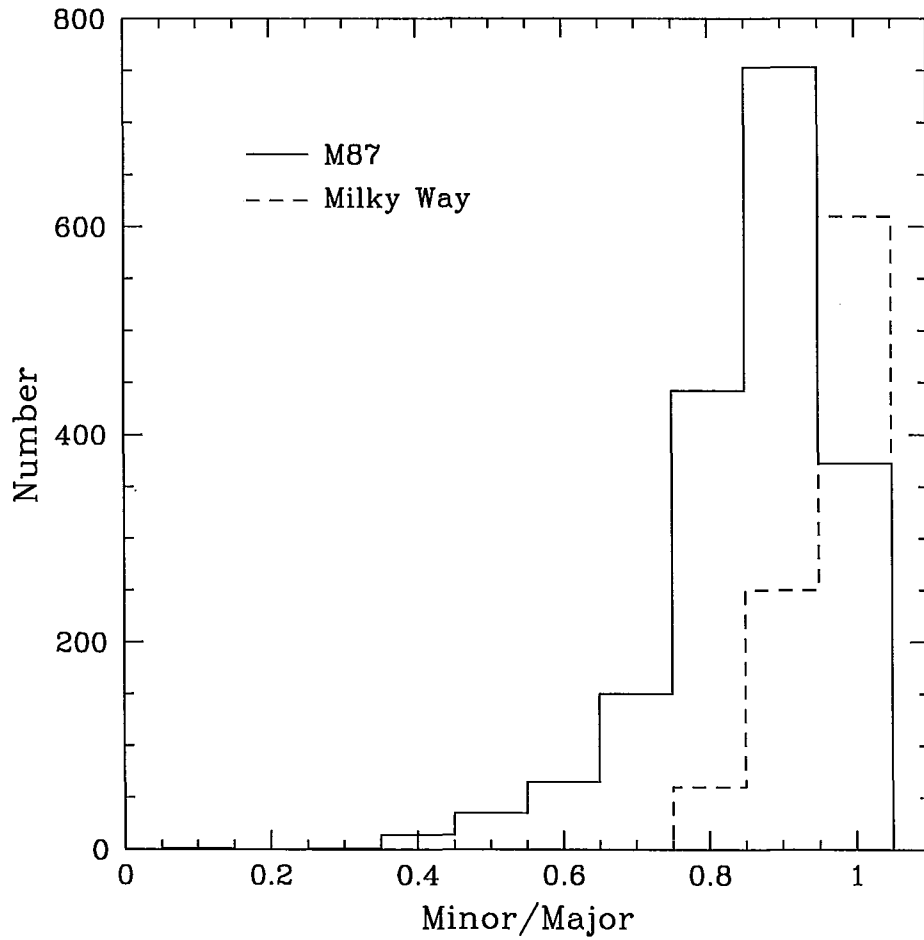


Figure 4.8 Values for the ratio of minor/major axis for the M87 clusters. Most clusters are nearly round ($e < 0.2$), although the mean ellipticity is slightly larger than in the Milky Way.

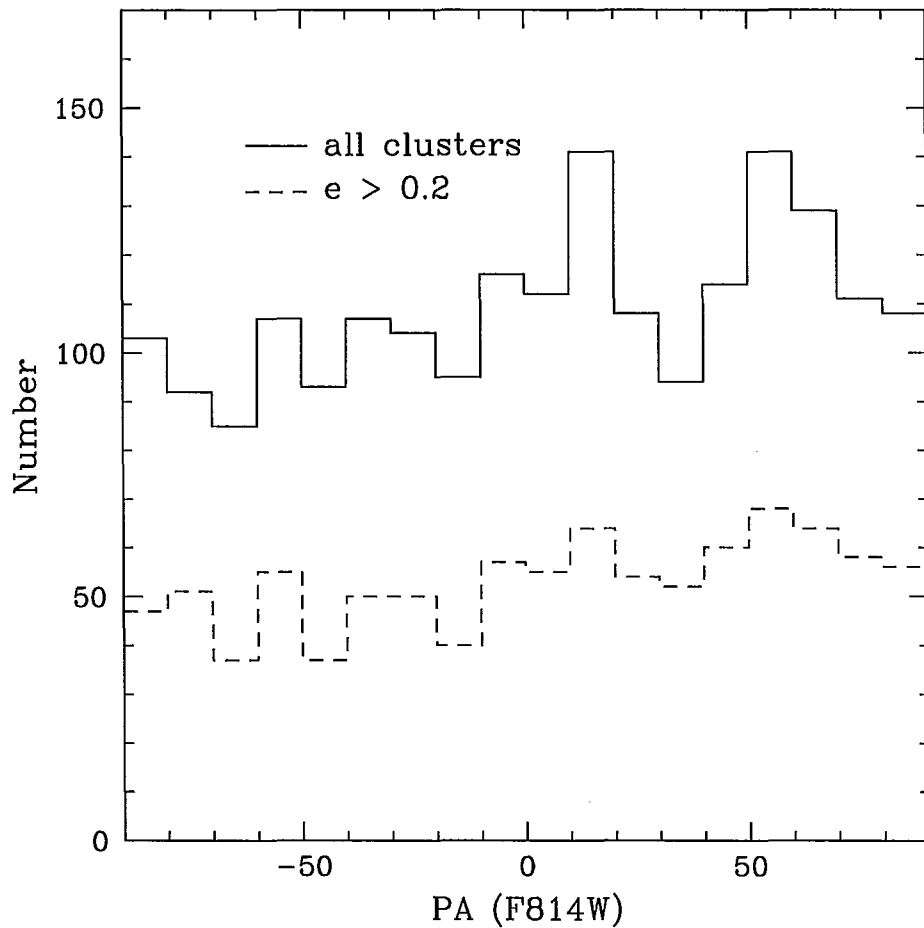


Figure 4.9 Histograms summarizing the values for the position angle of M87 clusters. The solid line represents the values taken by the position angle of all clusters. The dashed line corresponds to elongated clusters ($e > 0.2$) for which the position angle has a greater physical meaning.

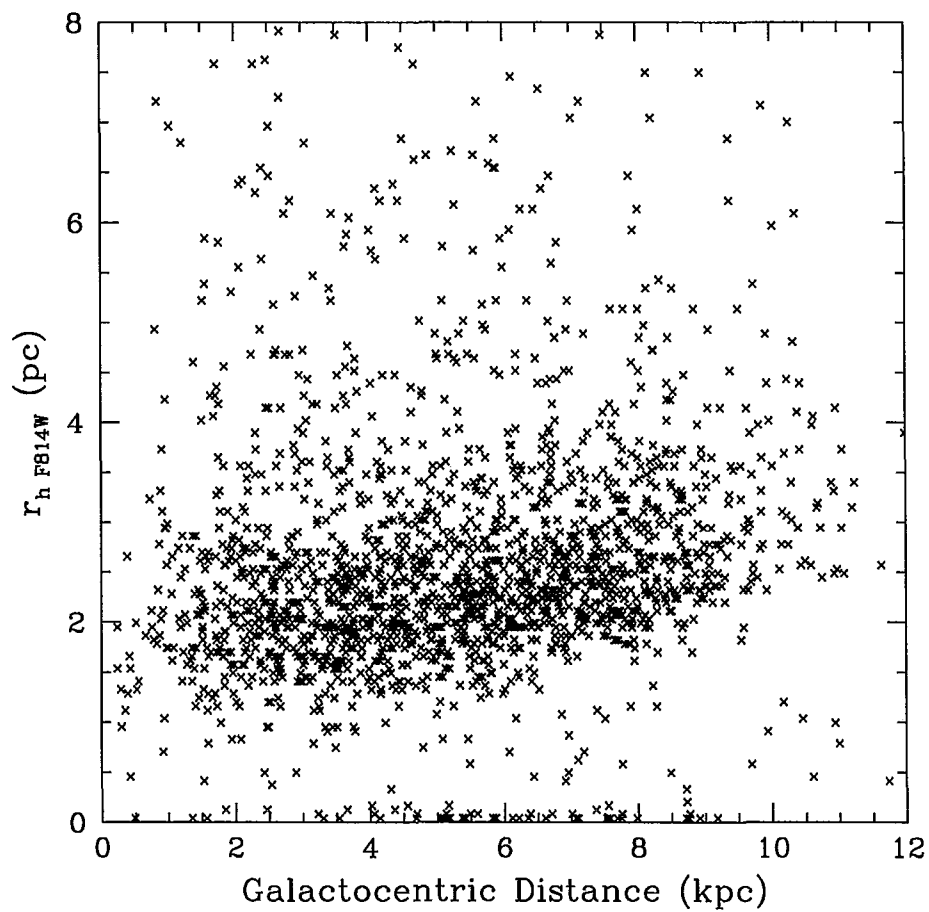


Figure 4.10 Effective radius, in the F814W filter, versus galactocentric distance. Note the small number of starlike objects scattered along the bottom of the graph, clearly separated from the globular cluster population.

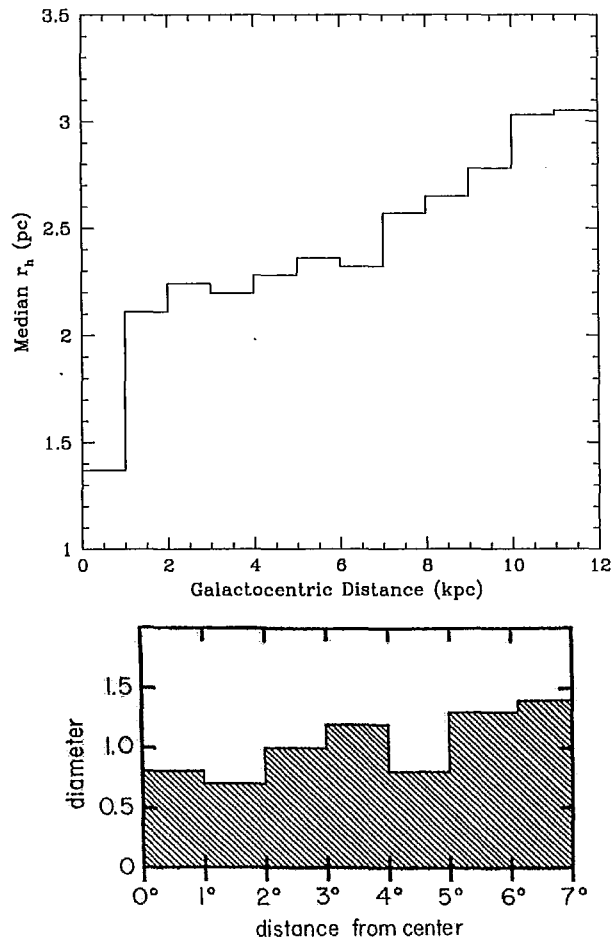


Figure 4.11 Median value of the effective radius (r_h) as a function of galactocentric distance (top). The histogram above recreates the historical histogram of Hodge (1962) where he plotted the sizes of clusters of the Large Magellanic Cloud vs. galactocentric distance (bottom).

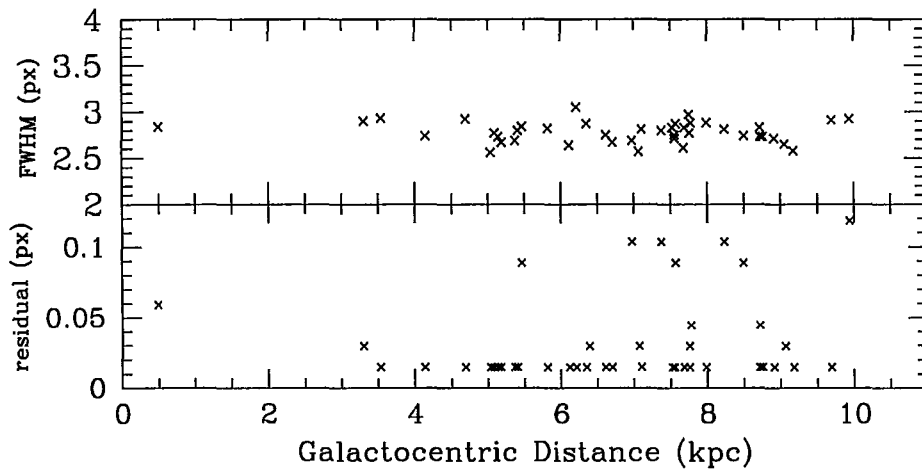


Figure 4.12 FWHM of sources with zero effective radius vs. galactocentric distance as measured with IMEXAMINE, top panel. The bottom panel shows the residuals of the PSF and the stars across the detector. We do not see any correlation of PSF size with position on the image.

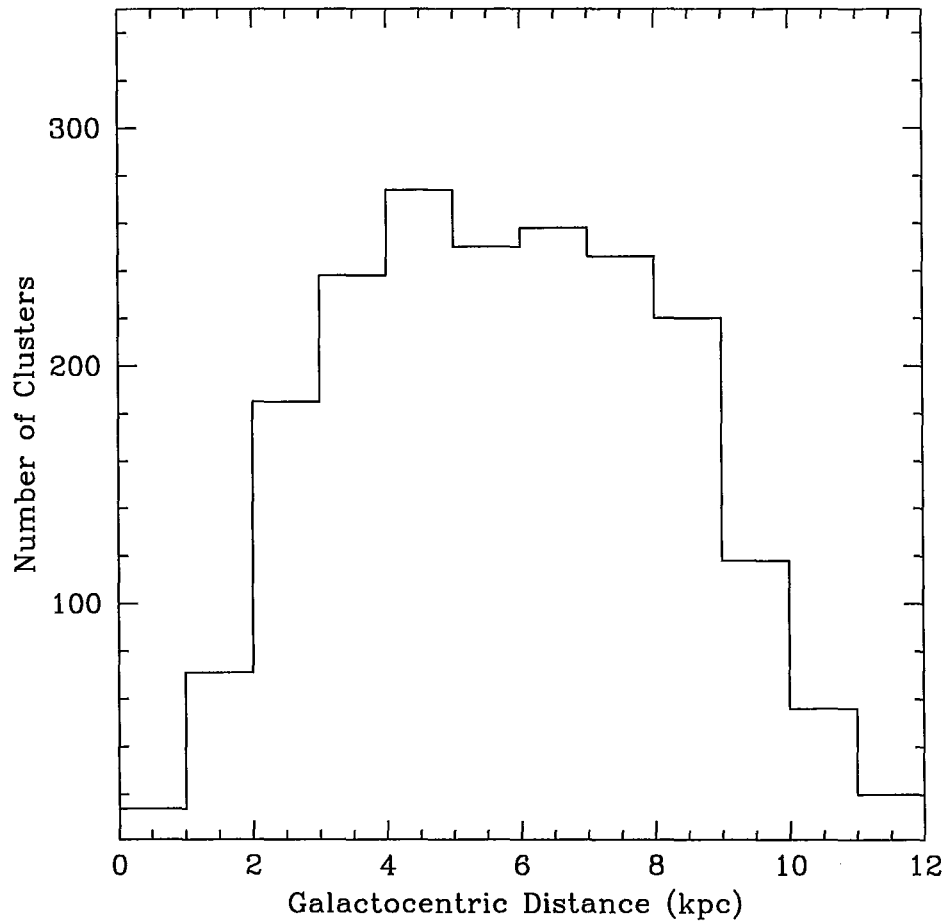


Figure 4.13 Number of globular clusters as a function of galactocentric distance.

Chapter 5

Color-Magnitude Diagram

5.1 Photometry

The photometry section of this thesis is placed after the study of the structural parameters to better reflect the steps we followed in our analysis. Indeed, we calibrate our photometry *after* we obtain the effective radius for our clusters as follows.

We determine the magnitudes on the output images of APSIS using the expression:

$$m_{VEGA} = -2.5\log(FLUX \times CORRECTION) + 2.5\log(EXPTIME) + ZP$$

where FLUX is the number of counts within a circular aperture of 5 pixels (0.175") in radius. CORRECTION is the aperture correction factor that we apply and that we describe below. EXPTIME is the total exposure time in seconds for each image and ZP is the zeropoint in the VEGAMAG system.

The VEGAMAG system is defined by normalizing the flux of the object to the flux of Vega (α Lyr) thus:

$$VEGAMAG = -2.5 \log\left(\frac{FLUX}{F_{VEGA}}\right)$$

In the VEGAMAG system Vega has a magnitude of zero at all wavelengths.

Our data was taken before the failure of the ACS Side 1 electronics and following temperature change of the camera in 2006 June (Sirianni et al. 2006). The corresponding photometric zeropoints are obtained from the STScI website: $ZP_{F606W} = 26.420$ and $ZP_{F814W} = 25.536$.

To calculate the aperture correction we used the procedure below. Using the ISHAPE tasks MKCMPPSF and MKSYNTH we create model images of synthetic globular clusters. We make these synthetic clusters with different profiles of varying intrinsic FWHM, and convolve them with the PSF. In order to recreate the sizes we obtained for the effective radius, we built clusters with FWHM from 0 to 3 pixels in steps of 0.02 pixels. These synthetic clusters have different curves of growth that we plot in Figure 5.1. With the curves of growth for these synthetic point sources, of known FWHM, we can perform an accurate aperture correction by measuring the offset in flux (or magnitude) for each cluster size to a stellar PSF. In Figure 5.2 we plot the flux correction as a function of cluster FWHM.

Once we determine the offset to a stellar source we can apply the aperture correction of Sirianni et al. 2005. Given that the Sirianni et al. (2005) tables do not give an aperture correction for $r=0.175''$ we use an interpolated value, i.e.

0.8205 for F606W and 0.7985 for F814W. With the above method we obviate the objections of Kundu (2008) related to the use of a fixed aperture to measure the flux of clusters with different sizes. Kundu (2008) and Waters et al. (2009) claim that the M87 Color-Magnitude Diagram and its substructures derived by several authors suffer greatly from the effects of fixed aperture photometry on clusters with varying size. Here we address this issue directly by carefully incorporating the effect of each cluster size on its photometric measurement.

5.2 Color-Magnitude Diagram

We present our final color-magnitude diagram for the M87 globular clusters in Figure 5.3. We plot the F814W magnitudes in the y-axis since these are a better tracer of the cluster stellar mass. The CMD in Figure 5.3 is consistent with previously published M87 CMDs, particularly with the CMD derived by Larsen et al. (2001) using WFPC2 data and a similar pair of filters i.e. the F555W and the F814W.

5.2.1 Bimodality

The discovery of the bimodality in the color distribution of extragalactic globular cluster systems is perhaps the most important discovery in the field during the last decade (e. g. Brodie & Strader 2006). The color bimodality indicates the presence of two distinct subpopulations of globular clusters with different metallicities: a blue, metal-poor population $[\frac{Fe}{H}] < -0.8$, and a red, metal-rich population $[\frac{Fe}{H}] > -0.8$. These two subpopulations not only differ

in metallicity but in also in their spatial distribution and kinematics (West et al. 2004, and references therein). It has been shown that red clusters are more centrally concentrated than blue ones (Côté et al. 2001). Here, we study images of the inner regions of M87 and thus $\sim 60\%$ of the clusters we detect are red clusters, see Figure 5.7.

To date, this color bimodality has been ubiquitous in elliptical galaxies for which color-magnitude diagrams have been obtained. The origin of these two subpopulations as well as the implications of their existence in galaxy formation theory have been largely discussed in the literature. Several papers have addressed the question of how two subpopulations of clusters coalesce into one globular cluster system. One hypothesis to explain this bimodality postulates that metal-rich and metal-poor clusters originate in two separate episodes of star formation at high redshift. A primordial metal-poor subpopulation would originate simultaneously with the host galaxy while a second metal-rich subpopulation would arise from the mergers the galaxy undergoes during its billions of years of evolution (Ashman & Zepf 1992). It has been shown that mergers and interactions between galaxies trigger the formation of star clusters, see for instance, the study of M51 done by Whitmore and collaborators (e. g. Lee et al. 2005).

A second hypothesis to explain the presence of these two subpopulations claims that the metal-rich subpopulation is inherent to massive galaxies while the metal-poor subpopulation is accreted from smaller galaxies during the collisions and stripping of material leading to the formation of ellipticals (West et al. 2004). There is a correlation between galaxy mass and parent cluster

metallicity. This second hypothesis obviates the need of two episodes of cluster formation and is supported by the observations of tidal tails proving the exchange of stars and matter between galaxies. The two hypotheses described above are challenged by the diversity of possible scenarios of cluster formation currently observed which lead others to think that the current globular cluster systems are formed through a combination of the processes described above. Additional challenges to current theories of cluster formation come from observations of globular clusters that might be stripped nuclei of dwarf galaxies and from a probable population of intergalactic globular clusters (West et al. 2004).

In the case of M87 one can argue in favor of the two main formation scenarios described above (Harris et al. 1998): M87 has well documented dust/gas lanes, some of which are actually visible in this dataset (Sparks et al. 1993). Such dust/gas lanes might be the vestige of past “wet” mergers that triggered the formation of new clusters. On the other hand, M87 is the central dominant galaxy of the Virgo Cluster i. e. the space of the nearby Universe with the highest galaxy density. It has been shown that cannibalization of clusters from nearby galaxies during billions of years of evolution can build the bimodal GCS of M87 (Harris et al. 1998, and references therein).

The sharpness of the M87 bimodality is striking and is more clearly defined than in previous work (e. g. Larsen et al. 2001, Peng et al. 2006) because of the much higher S/N of this deep dataset. In the magnitude range $F814W \simeq 22.0 - 22.5$ we note a “bridge” between the normal blue and red sequences, with many more clusters than usual at intermediate colors. These clusters

are randomly distributed in the field. They may be genuinely intermediate-metallicity objects. Given the age/metallicity degeneracy for old clusters they might also be metal-rich but younger by a few Gigayears than the red sequence clusters. Strader et al. (2006) note the presence of this bridge using shallower ACS data of M87, they record an H -like structure for the CMD of M87 and M49 as well.

5.2.2 Comparison with the Waters et al. (2009) CMD

The CMD presented here differs from the CMD derived by Waters et al. (2009) due to the reasons discussed in detail by Peng et al. (2009). One of the most evident differences is the presence in the Waters et al. (2009) CMD of bright ($I < 22$) clusters that are either very blue ($V - I < 0.9$) or very red ($V - I > 1.3$). The equivalent areas of our CMD are completely devoid of clusters, suggesting that the random errors in the magnitudes calculated from the curve-of-growth procedure are low while the scatter on the CMD derived by Waters et al. is very large. A detailed study of the CMD for the M87 GCS is presented by Peng et al. (2009).

5.3 Statistical Fitting

We use the software R for our statistical calculations presented in this work. R is a freely available, open source environment for statistical computing. The code RMIX, run within R, is specially designed to evaluate the mixture of statistical distributions of any given histogram. RMIX is partic-

ularly well suited for the analysis of the underlying distributions present in the color-magnitude diagram. RMIX is versatile and allows the user to set various parameters such as the best curve to fit the data (e. g. Gaussian, Poisson) and the type of dispersion (e.g. homoscedastic (same dispersion), heteroscedastic (different dispersion)). Documentation about RMIX can be found at <http://www.math.mcmaster.ca/peter/mix>.

We performed statistical fits for the whole distribution of the Color-Magnitude Diagram and for subsets of “horizontal cuts” as function of cluster magnitude ($F814W$). All fits presented here are based on color ($F814W-F606W$) bins of 0.05 of width in magnitude. It is evident that a single Gaussian is insufficient to fit the color distribution of globular cluster systems (Wehner et al. 2008). In Figures 5.3 and 5.4 we show the RMIX fit of two individual Gaussians to the data to the entire CMD, each Gaussian fits a subpopulation of clusters. The mean color for metal-poor clusters is $F606W - F814W = 0.66 \pm 0.02$ with a standard dispersion of $\sigma = 0.096 \pm 0.01$ while metal rich clusters have a mean color of $F606W - F814W = 0.85 \pm 0.01$ and $\sigma = 0.103 \pm 0.01$. The proportions of the metal-poor and metal-rich subpopulations are 36% and 64%, respectively.

Figure 5.5 shows histograms of “horizontal cuts” in the Color-Magnitude diagram by magnitude bin with their respective RMIX fit. These subsets have the following magnitude ranges in $F814W$: 20-21, 21-22, 22-23, and 23-24. The bimodality is sharp on the two top panels ($m_{F814W} = 20 - 21, 21 - 22$) while it is smeared on the lower two panels ($m_{F814W} = 22 - 23, 23 - 24$). The above effect is easily explained by large photometric errors creating a

Table 5.1 Results of RMIX fits to the Color-Magnitude Diagram

m_{F814W}	metal-poor			metal-rich			N Clusters
	%	mean	σ	%	mean	σ	
20-21	59%	0.68 ± 0.01	0.06 ± 0.01	41%	0.87 ± 0.01	0.04 ± 0.01	222
21-22	53%	0.73 ± 0.04	0.09 ± 0.02	47%	0.92 ± 0.02	0.05 ± 0.01	443
22-23	36%	0.69 ± 0.01	0.08 ± 0.01	64%	0.91 ± 0.01	0.09 ± 0.01	644
23-24	16%	0.62 ± 0.04	0.09 ± 0.02	84%	0.88 ± 0.02	0.14 ± 0.01	394

spread on the colors of faint clusters with $m_{F814W} \sim 22.5 - 24$. A more detailed analysis would be required to establish a color-magnitude relation for this data, however we can point out based on our fits that in Figure 5.5 the location of the mean for metal-poor population (left Gaussian) shifts towards the red with decreasing magnitude. The numerical results of the RMIX fits are summarized in Table 5.1. In this table we present for both metal-poor and metal-rich subpopulations its proportion of clusters per magnitude bin, their mean color, standard deviation σ , and the total number of clusters.

Interestingly, the best fit for clusters belonging to the magnitude range $m_{F814W} = 19 - 20$, i. e. the brightest clusters of the CMD, is a unimodal distribution *not* a bimodal distribution. In fact, the reduced χ^2 * is $\chi^2 = 0.85$ for a unimodal distribution while $\chi^2 = 0.88$ for a bimodal distribution. The best fit Gaussian has a mean color of 0.77 ± 0.01 and a standard deviation $\sigma = 0.10 \pm 0.01$. Even if the goodness of fit is very similar for both unimodal and bimodal distributions in this magnitude interval, thus preventing definitive

* the reduced χ^2 corresponds to χ^2 divided by the number of degrees of freedom

conclusions, we should mention that Dirsch et al. (2003) find that the brightest clusters of NGC1399 also have a unimodal distribution.

In addition we performed a statistical fit to clusters belonging to the magnitude range where the “bridge” of potential intermediate metallicity clusters is located on the CMD i. e. $m_{F814W} = 21.5 - 22.5$. We fitted the color distribution of clusters in this magnitude bin with both two and three Gaussians, bimodal and trimodal distributions. The goodness of fit dramatically improves with the addition of a third Gaussian to the fit of the distribution: the reduced χ^2 is, for a bimodal distribution, $\chi_{bimodal}^2 = 5.97$ while for a trimodal distribution $\chi_{trimodal}^2 = 1.21$. However, the trimodal fitting of the distribution shows that only 6% of clusters in the magnitude range $m_{F814W} = 21.5 - 22.5$ belong to this third intermediate subpopulation with the blue and red subpopulations accounting for 43% and 52% of the total color distribution, respectively. The actual RMIX fit is shown in Figure 5.6 where the third Gaussian added to improve the fit is a the wide Gaussian at the bottom of the graph. This is an interesting finding since there is no documented statistical evidence of the existence of a third mode in the literature. Further tests to the physical reality of this third mode, as described in Chapter 7, are justified.

Colors of the Space Telescope magnitude system (F606W-F814W) can be converted to $V - I$ by following the formula (de Graaff et al. 2007):

$$(V - I) = 1.2(m_{F606W} - m_{F814W}) + 0.06.$$

5.4 Effective Radius versus Magnitude

In Figure 5.7 where we plot magnitude versus effective radius for metal-poor and metal-rich clusters, the boundary between red and blue clusters is set at $F814W-F606W >$ or $<$ than 0.8. In this figure we can see how metal poor clusters have larger r_h than their metal rich counterparts. Red clusters have a median r_h of 2.1 pc while for blue clusters the median r_h is 2.6 pc. Blue clusters are thus on average 24% larger than red clusters, this offset is in excellent agreement with the findings of previous studies using large cluster samples in other galaxies (e. g. Larsen et al. 2001, Spitler et al. 2006, Harris 2009). The r_h median value is not affected by the presence of clusters with $r_h \sim 0$ visible at the bottom of the two graphs of Figure 10. This size difference between subpopulations was explained by Jordán (2004) as the result of mass segregation and the dependence of main-sequence lifetimes on metallicity. Another possibility is that this difference reflects conditions of formation, the abundance of chemical elements play a dominant role in the heating and cooling functions of the ISM and thus can have great influence in the formation of clusters from molecular clouds. We do not observe any clear trends of increasing (or decreasing) r_h with magnitude. The HST proposal submitted during cycle 17 (Chapter 4) was aimed at measuring the size difference between metal-poor and metal-rich clusters at large R_{GC} . The evolution with R_{GC} of the size difference between the two subpopulations can help to distinguish between competing hypotheses explaining its origin, particularly clarifying the influence of the host galaxy tidal field.

One clear fact evident in Figure 5.7 is the unfilled space between 0 and ~ 1.5 pc in both plots at all magnitudes except the faint end. As we pointed out in Chapter 4 this gap between the unresolved stars and the smallest clusters is also visible in Figures 4.3, 4.4, & 4.10. It appears as most clusters have a minimum effective radius. This gap in the r_h distribution is also present in previous studies of M87 (Kundu et al. 1999, Larsen et al. 2001). Of the Cen A and Milky Way clusters none has been reported with an effective radius of less than 1pc (Gómez et al. 2006, Gómez & Woodley 2007).

An explanation for the existence of this is gap, or minimum effective radius is that smaller clusters have a smaller chance of survival. McLaughlin & Fall (2008) study the relation of the globular cluster mass function and the cluster half-mass density (ρ_h). In their study, these authors normalize the disruption time of a globular cluster to the relaxation time and find that the evaporation rate μ_{ev} is proportional to $\rho_h^{1/2}$. Using their relation between ρ_h and the effective radius we can write $\mu_{ev} \propto r_h^{-3/2}$. This means that smaller clusters evaporate much faster than bigger ones (Fall & Rees 1977, 1985). The evaporation rate determined by McLaughlin & Fall (2008) only takes into account internal relaxation effects, however. The influence of an external potential on the dissolution timescale is examined by Gieles & Baumgardt (2008). These authors conclude that in the presence of a tidal field the dissolution time scales with the number of stars in the cluster N and the angular frequency ω of the cluster in the host galaxy: $t_{dis} = \frac{N^{0.65}}{\omega}$.

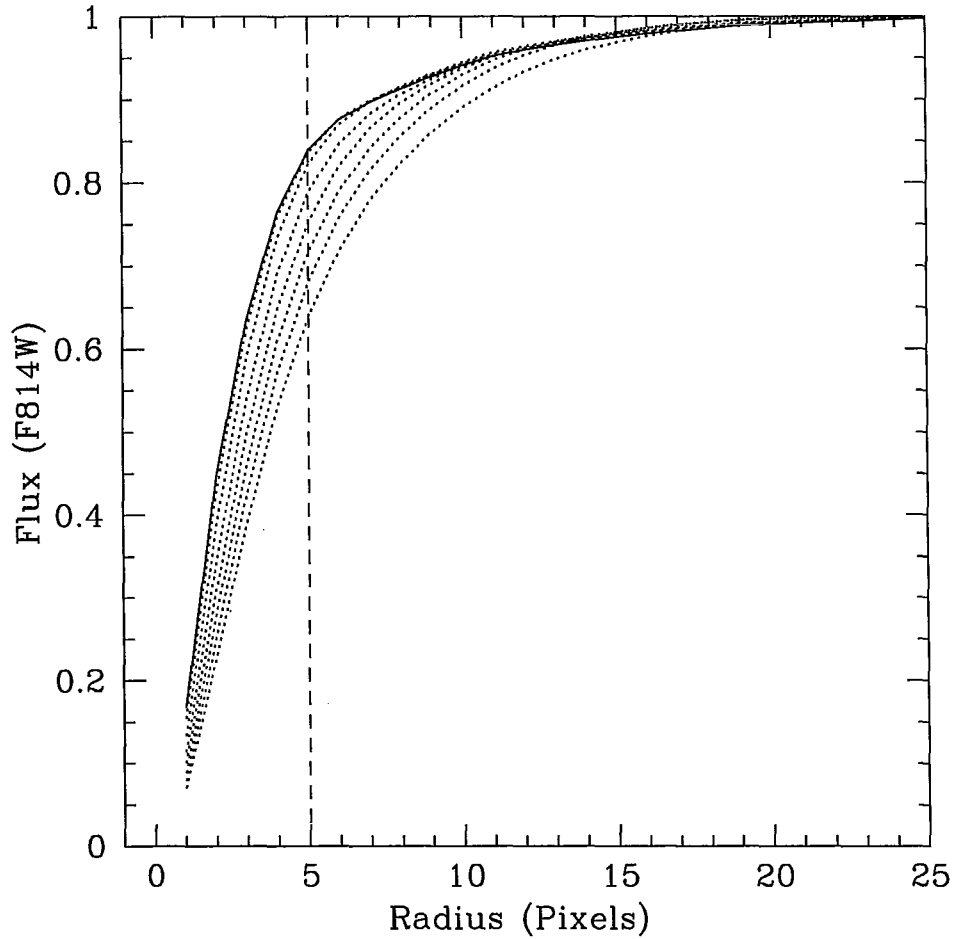


Figure 5.1 Curves of growth for synthetic sources (globular clusters) of different FWHM. The solid line corresponds to a source with FWHM=0, i.e. a starlike object. The dotted lines show the curves of growth of seven sources with FWHM varying from 0 to 1.4 pixels (in steps of 0.2 pixels) convolved with the PSF. The vertical dashed line at 5 pixels marks the radius of the circular aperture we used for our photometry.

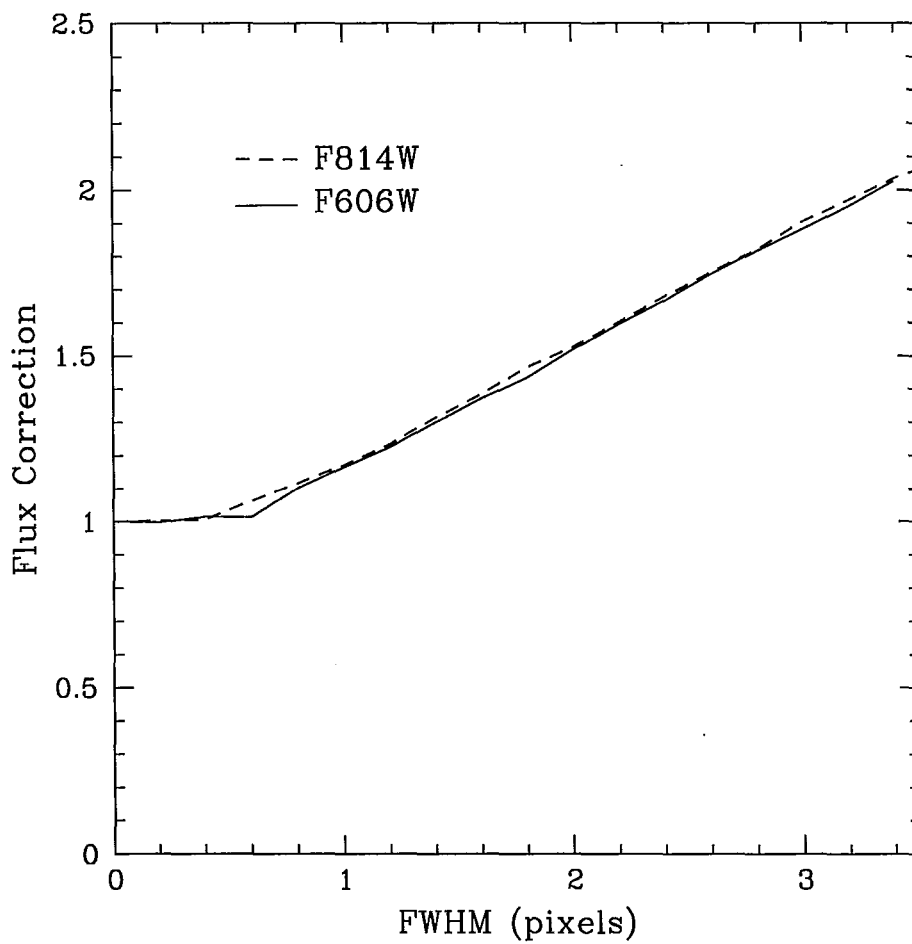


Figure 5.2 Flux correction as a function of cluster FWHM.

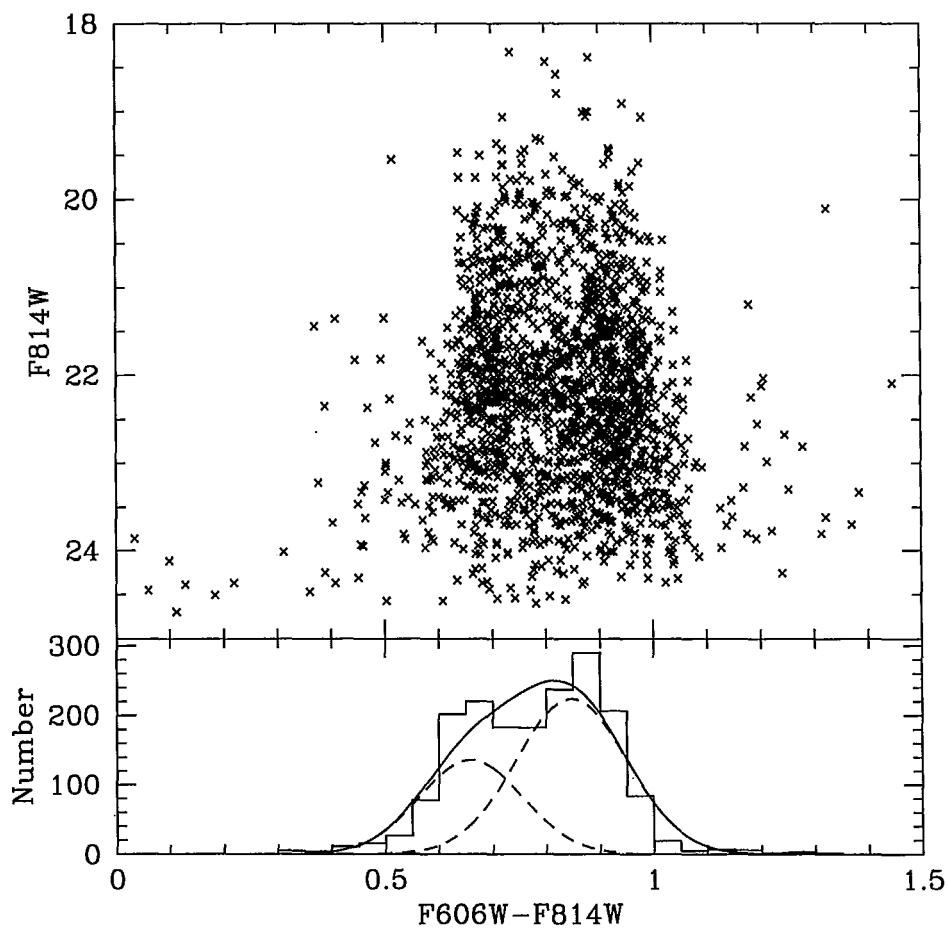


Figure 5.3 Color-magnitude diagram (top) and histogram of cluster colors (bottom) for the M87 Globular Cluster System, the sharpness of the bimodality is striking.

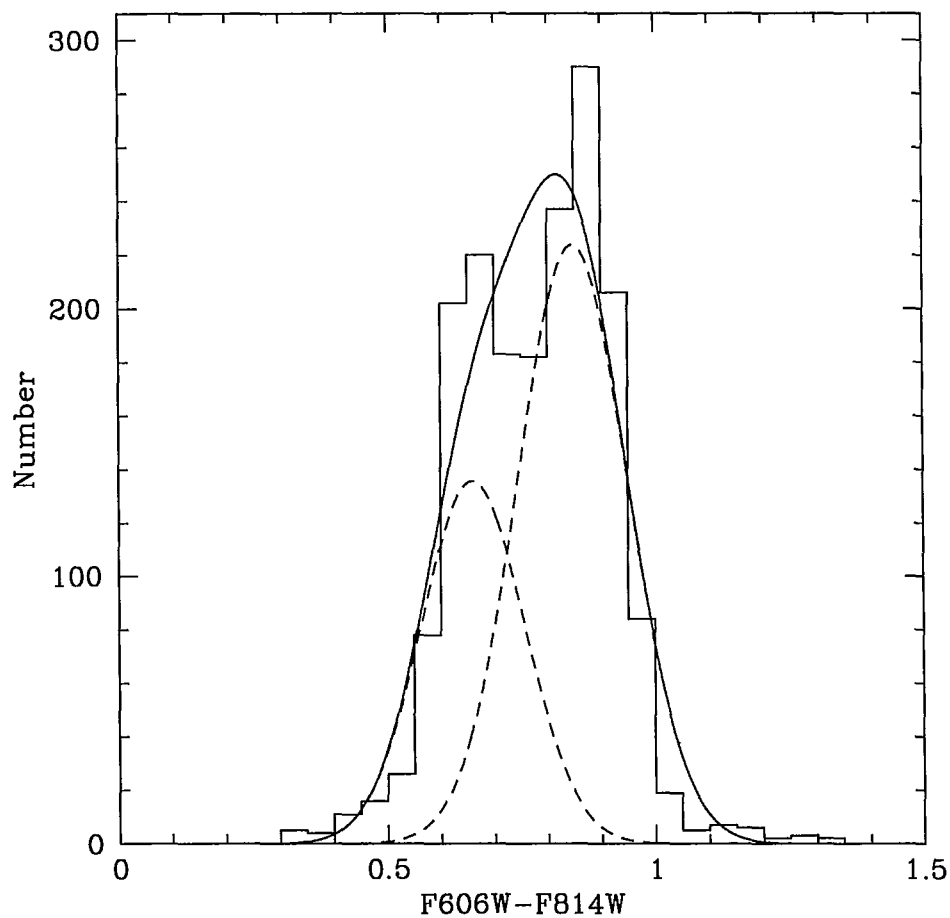


Figure 5.4 Color distribution of globular clusters with Gaussians resulting from the RMIX fit to the data. The dashed lines correspond to the individual fit of the metal-poor and metal-rich subpopulations. The solid line is the sum of the two individual populations.

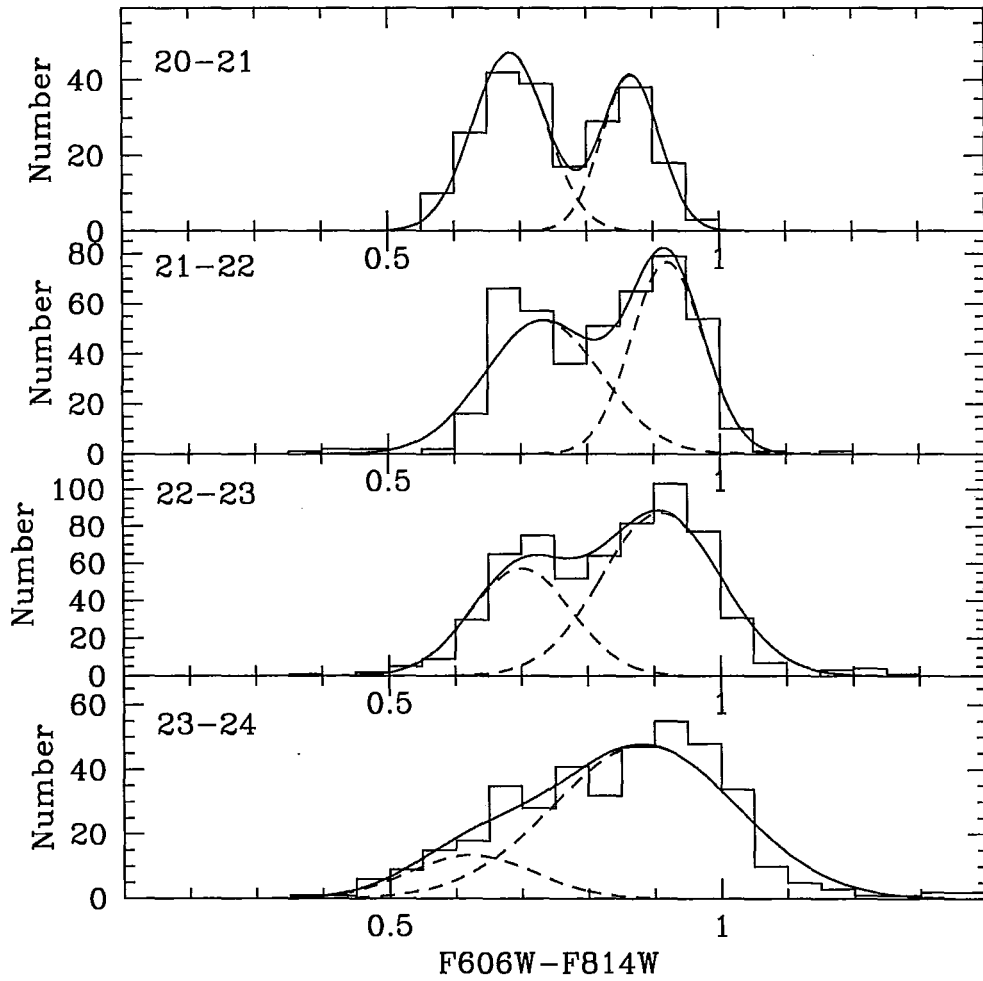


Figure 5.5 Histograms and RMIX fits to the CMD for different magnitude bins. The magnitude interval is indicated on the upper left of each panel.

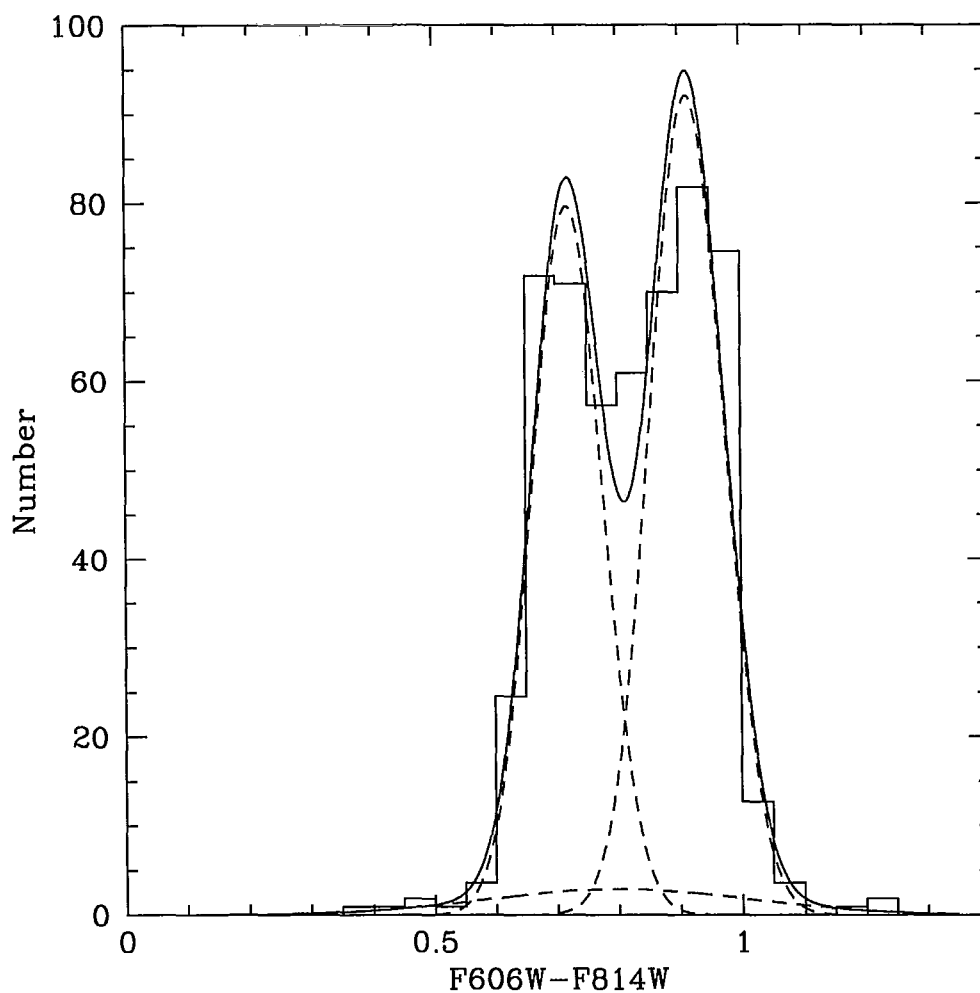


Figure 5.6 Color distribution of Globular clusters between $m_{F814W} = 21.5$ and $m_{F814W} = 22.5$, this is the magnitude range where a "bridge" between red and blue subpopulations is located. The third Gaussian accounting the existence of the bridge is the wide curve near the bottom of the graph.

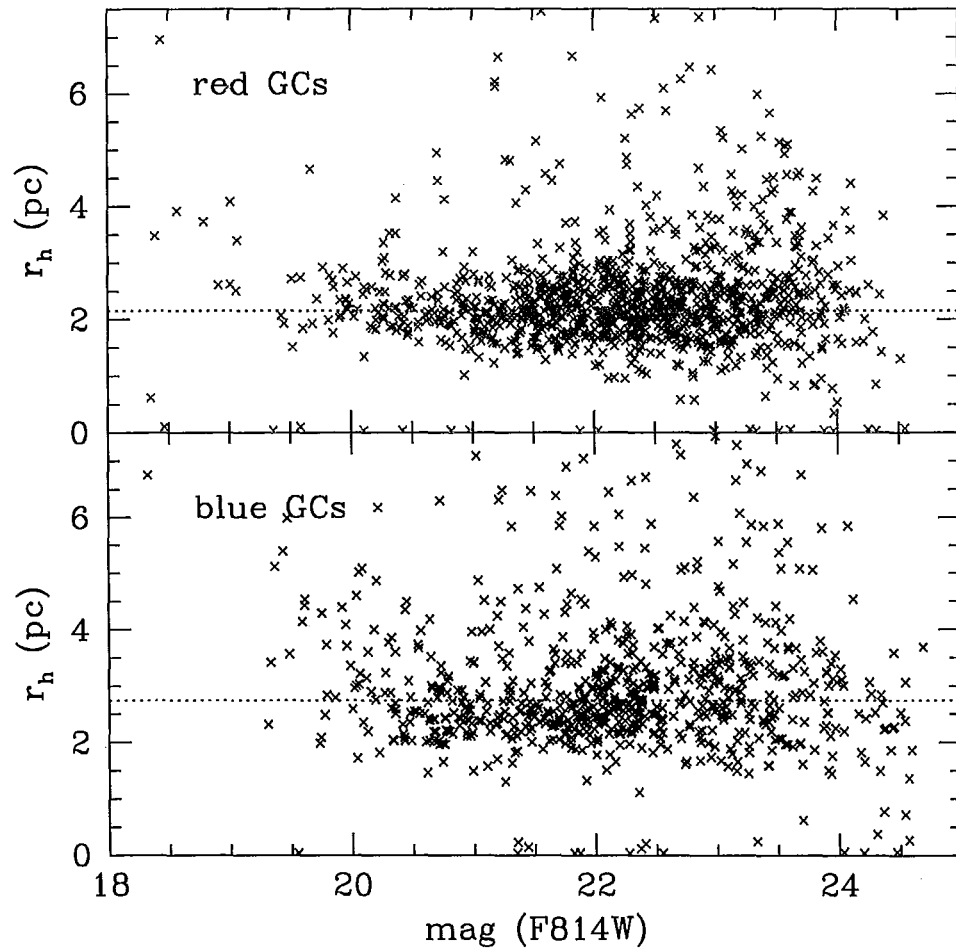


Figure 5.7 Effective radius versus magnitude for the two, red and blue, sub-populations of globular clusters. The dotted line represents the median value for the r_h of each subpopulation.

Chapter 6

Globular Cluster Luminosity Function for M87

6.1 Globular Cluster Luminosity Function

For a given galaxy or Globular Cluster System the number of clusters per unit magnitude defines the Globular Cluster Luminosity Function (GCLF) (Harris 2001). For giant elliptical galaxies the GCLF can be accurately described by a Gaussian function with a mean value of $M_V^0 = -7.21 \pm 0.26$ mag and a standard deviation of $\sigma = 1.35 \pm 0.05$ mag (Whitmore 1997). The mean value of $M_V^0 = -7.21 \pm 0.26$ corresponds to roughly a mass of $\sim 2 \times 10^5 M_\odot$ at the turn over (Jordán et al. 2007). In spirals the mean value remain the same but with a smaller dispersion $\sigma \sim 1.2$ (Brodie & Strader 2006). The Gaussian shape and the turnover magnitude (M_V^0) appear to be universal. The similarity between the GCLFs of two vastly different galaxies such as, for instance, the Milky Way and M87 is truly surprising (Ashman & Zepf 1998). These properties have been used to exploit the GCLF as a standard candle in the Local Universe, particularly with HST observations. Using HST the GCLF

can be used as a distance estimator up to 250 Mpc. In fact, the superior resolution and sensitivity of HST drastically improved the data available to build GCLFs. HST allows to reach 2 to 3 magnitudes beyond the turnover at the distance of the Virgo Cluster. Before HST, only the brightest clusters up to the turnover were detectable (e.g. Couture et al. 1990, Whitmore 1997).

In Figure 6.1 we show the Globular Cluster Luminosity function for M87. No fitting is overplotted with the histogram to prevent the illusion of perfect symmetry. GCLFs are naturally skewed with missing clusters on the faint end of the distribution. Our requirement of $S/N > 50$ for all clusters aggravates this incompleteness on the faint end. However, Figure 6.1 shows that even with conservative requirements on the signal to noise this dataset has a detection limit 3 magnitudes beyond the turnover. We use the following transformations to convert to magnitudes in the I band (de Graaff et al. 2007):

$$I = m_{F814W} + 25.495 - 0.002(V - I)$$

$$(V - I) = 1.2(m_{F606W} - m_{F814W}) + 0.06$$

The I band is more representative of cluster mass and is thus preferred over the V band for our representation of the GCLF.

We used RMIX to find the best fit to the GCLF which we plot in Figure 6.2. Historically, and usually, the GCLF has been fitted with a Gaussian function, however, some authors have introduced other functions e. g. Evolved Schechter function (Jordán et al. 2007) that takes into account the asymmetry of the luminosity function and the underlying physical reasons that explain the

mass function for globular clusters. Also, Secker (1992) claimed that the best fit to the Milky Way GCLF was obtained by using a Student's t_5 function.

In Figure 6.2 the histogram of 1812 globular clusters is overplotted with the best fit Gaussian function with a mean of $m_{F814W} = 22.14 \pm 0.03$ and a dispersion of $\sigma = 1.14 \pm 0.02$. This result was obtained by constraining the fit to the median value calculated beforehand, to allow us to minimize the effect of incompleteness of the luminosity function faint end on the fit itself. Peng et al. (2009) derive a GCLF and respective fits for the entire Globular Cluster system and its two subpopulations. Peng et al. (2009) find that the best Gaussian fit parameters for the luminosity function of the entire GCS are $m_{TO} = 22.53 \pm 0.05$ and $\sigma = 1.37 \pm 0.04$. The sample of clusters fitted by Peng et al. (2009) is larger (2250 clusters) than the sample used here (1812 clusters) due to different requirements on the signal-to-noise ratio in the two studies. Most clusters eliminated on our analysis are clusters with $S/N < 50$, these clusters clearly have the effect of shifting the mean to fainter magnitudes in the fit of Peng et al. The signal to noise requirements are set accordingly with the software used to derive the size estimates for clusters, i.e. the minimum signal to noise for an optimal size measurement is dictated by the software used to carry out the fits and not cluster flux. However, cluster size and flux are ultimately linked through the size-dependent flux correction we discussed in Chapter 5. Even if a better fit to the GCLF can be achieved with a looser requirement for the S/N the quality of ISHAPE fits would have been degraded, a harmful consequence given that the main focus of this work is the study of structural parameters.

6.2 Metal-poor and Metal-rich GCLF

It was shown in the previous chapter that the M87 globular cluster system is composed of two distinct sub-populations: one is a metal-poor (blue) sub-population and the other is a metal-rich (red) sub-population. We present the luminosity functions and their respective RMIX fits for both sub-populations in Figures 6.3 and 6.4. These two Figures and the results summarized in Table 6.1 suggest that the two sub-populations have different peak magnitudes and different widths. The metal-poor subpopulation appears to have a brighter peak than the metal-rich subpopulation m_{TO} blue = 22.11 ± 0.04 vs. m_{TO} red = 22.16 ± 0.03 . This finding is in agreement with Peng et al. (2009) who find a mean for metal-poor clusters of 22.24 ± 0.06 while metal-rich clusters peak at 22.77 ± 0.09 . The widths of the distribution of the two subpopulations are also different: we find a dispersion for metal-poor clusters of $\sigma_{blue} = 1.17 \pm 0.03$ while the dispersion for metal-rich clusters is $\sigma_{red} = 1.12 \pm 0.02$. Peng et al. (2009) find a larger dispersion for both sub-populations given their larger dataset which includes more clusters at the faint end i.e. $\sigma_{blue} = 1.25 \pm 0.05$ and $\sigma_{red} = 1.45 \pm 0.06$. The main difference with Peng et al. (2009) is in the values for the red subpopulation which is the most affected by incompleteness. Note that the results presented here correspond to an average across the (small) ACS field. Tamura et al. (2006b), using the Subaru/Suprime Cam wide field imager, showed that the color distribution of the globular cluster system of M87 varies as a function of radius.

An interesting application of the peak magnitude for each subpopulation of clusters is given in Puzia et al. (1999). These authors use the peak magni-

Table 6.1 Results of RMIX fits to the Globular Cluster Luminosity Function

	all clusters	metal-poor	metal-rich
N clusters	1812	756	1056
fixed mean			
mean	22.14 ± 0.03	22.11 ± 0.04	22.16 ± 0.03
σ	1.14 ± 0.02	1.17 ± 0.03	1.11 ± 0.02
fitted mean			
mean	22.14 ± 0.03	22.10 ± 0.04	22.17 ± 0.03
σ	1.14 ± 0.02	1.17 ± 0.03	1.12 ± 0.02

tude, or turnover, for each subpopulation as its *mean* magnitude. This mean magnitude combined with the mean color, which we derive in detail in Chapter 5, can be applied to find the age and metallicity of clusters based on stellar population synthesis models. There is a need to combine both mean color and mean magnitude due to the age-metallicity degeneracy. Puzia et al. (1999) conclude that the two subpopulations of clusters in NGC4472 formed in two major events only a few Gyr apart.

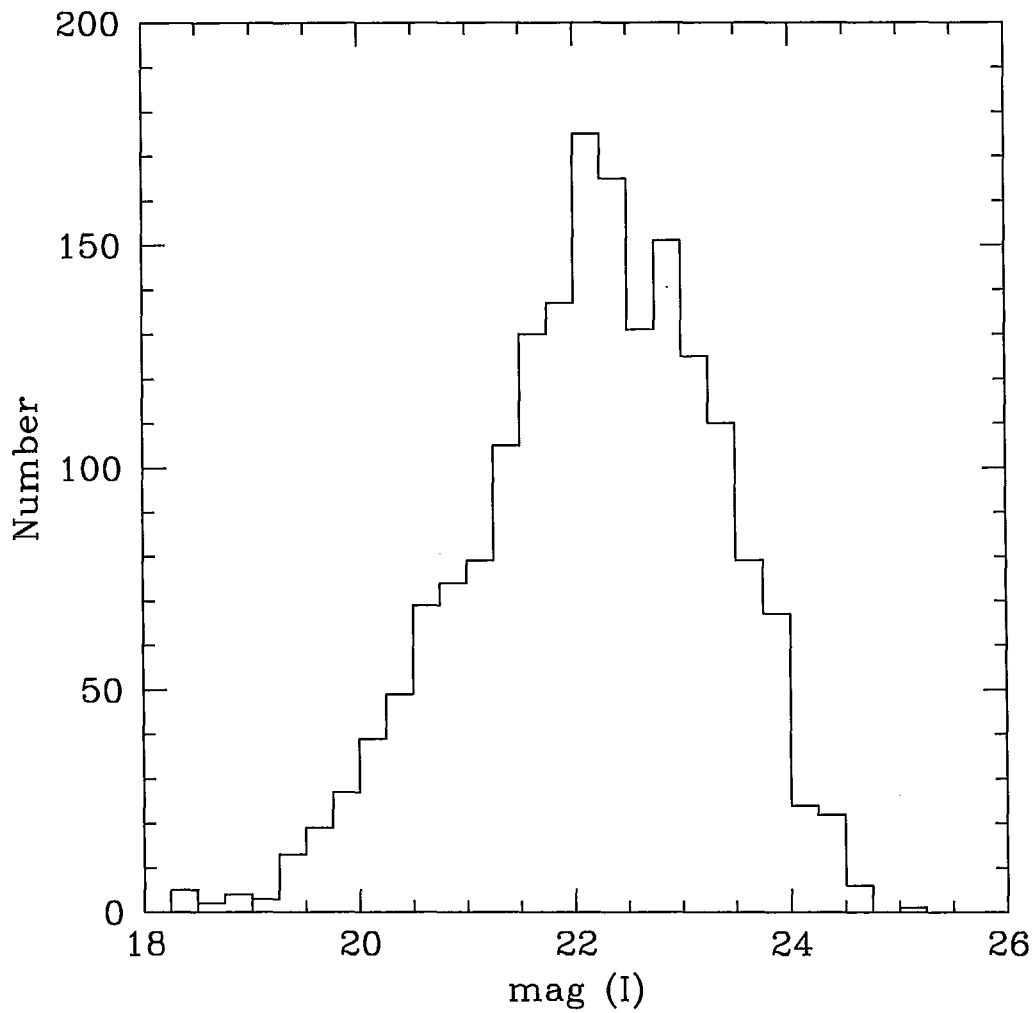


Figure 6.1 Globular Cluster Luminosity Function of M87. This Figure shows the asymmetry of the GCLF and the effect of incompleteness at the faint end of the distribution.

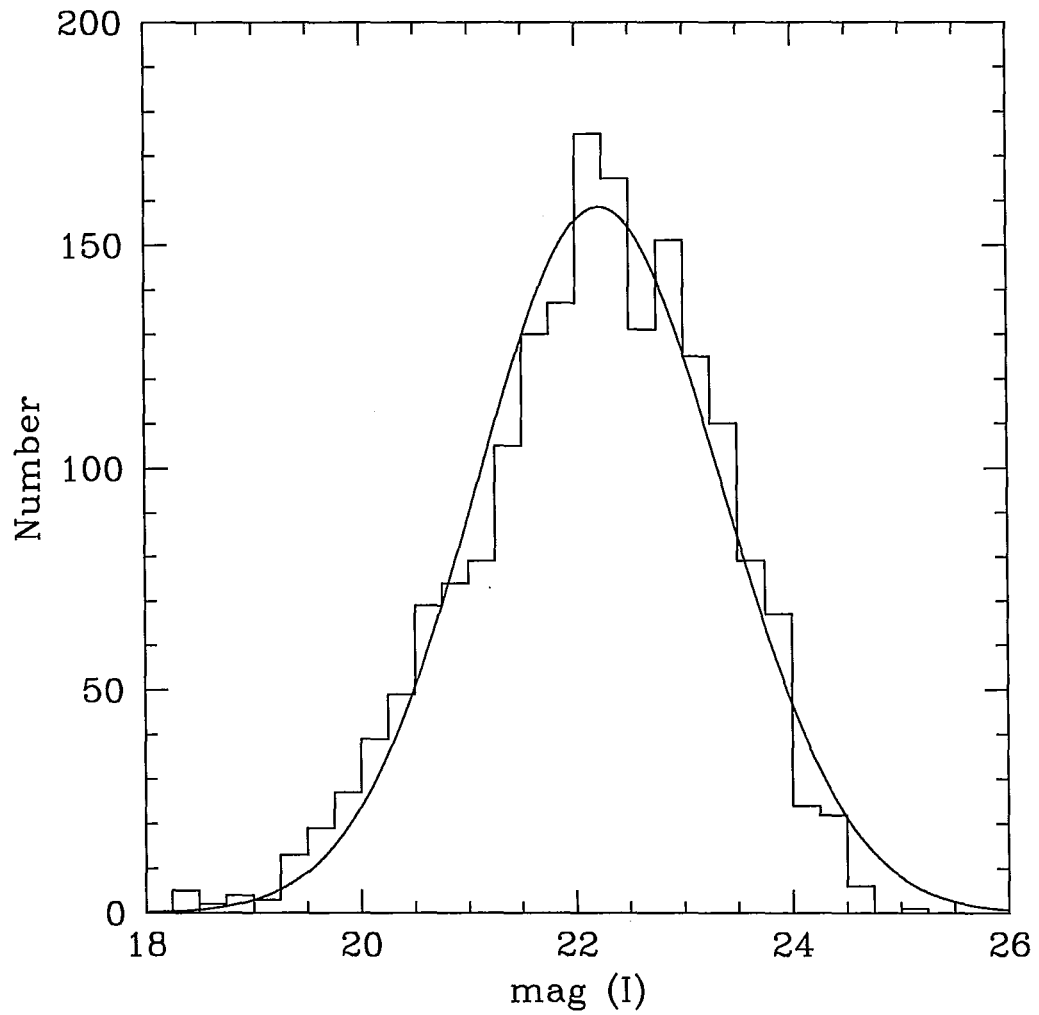


Figure 6.2 Globular Cluster Luminosity Function of M87, histogram and RMIX fit. The best fit to the distribution is a Gaussian with mean color of 22.14 ± 0.03 and standard deviation of $\sigma = 1.14 \pm 0.02$.

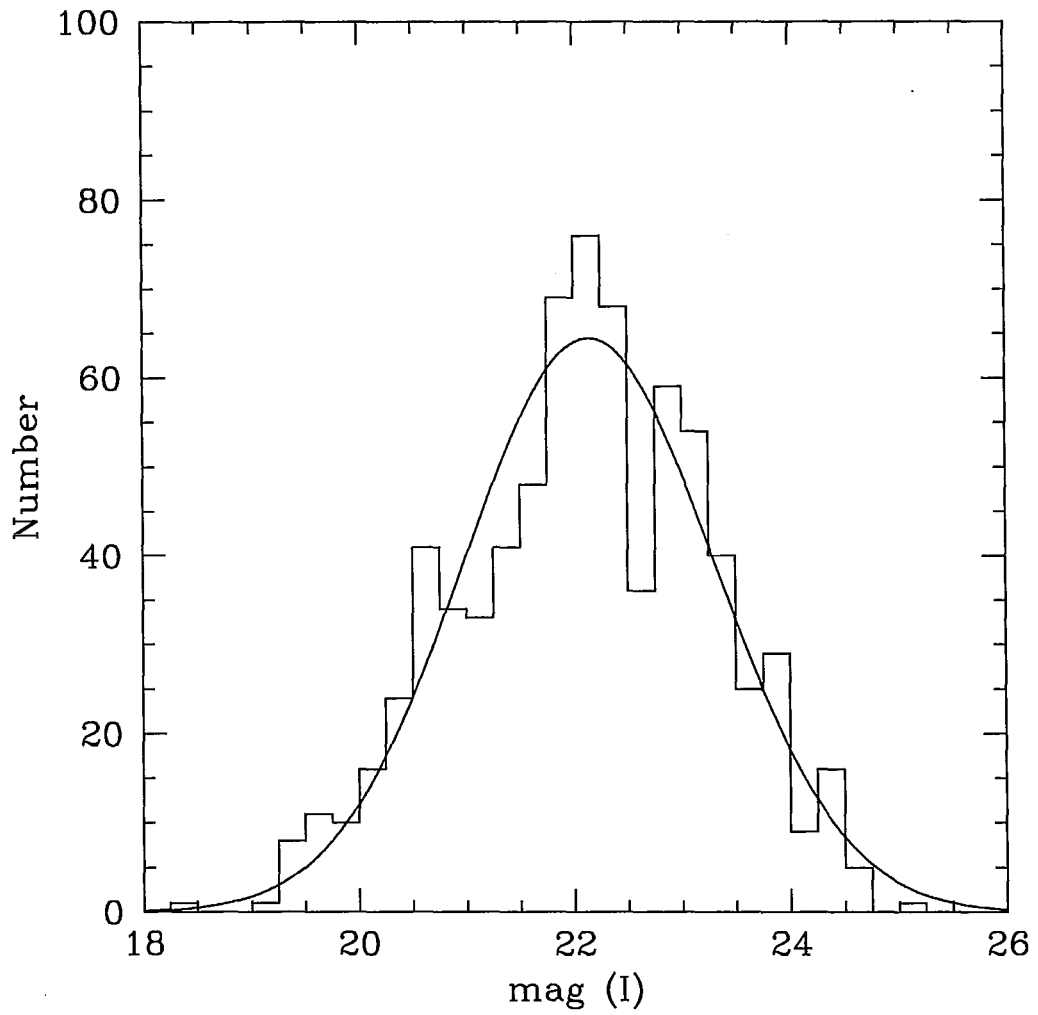


Figure 6.3 Globular Cluster Luminosity Function for the metal-poor sub-population. The mean color is 22.11 ± 0.04 and the standard deviation $\sigma = 1.17 \pm 0.03$.

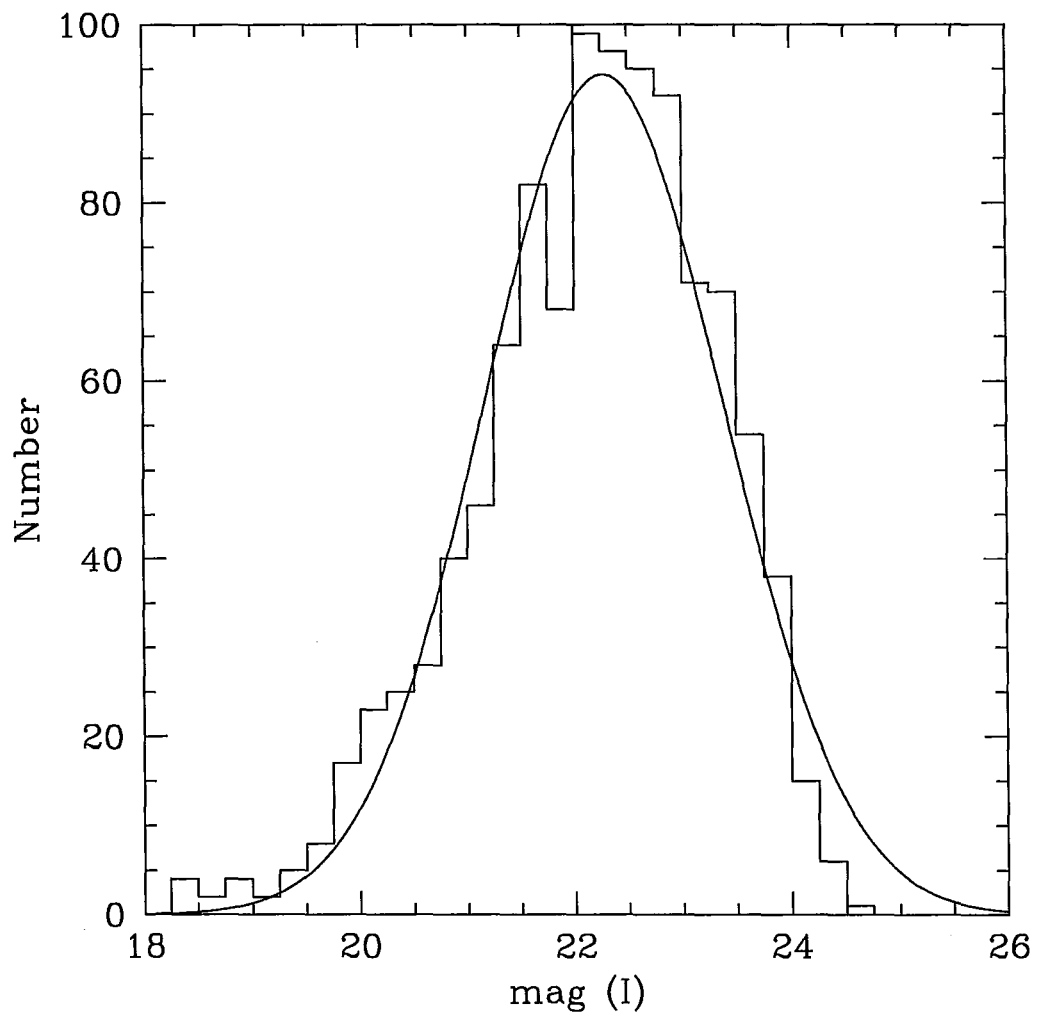


Figure 6.4 Globular Cluster Luminosity Function for the metal-rich subpopulation. The mean color is 22.16 ± 0.03 and the standard deviation $\sigma = 1.11 \pm 0.02$.

Chapter 7

Summary and Future Prospects

With extremely deep HST/ACS data in V and I, we have obtained precise measurements of the scale radii r_h for ~ 2000 globular clusters in M87. To first order, their size distribution closely resembles the Milky Way GCS, i. e. most clusters have effective radii between 1 and 6 pc. We find that the mean cluster size depends noticeably on both metallicity and galactocentric distance. Metal rich clusters are 24% larger and slightly fainter than the metal-poor subpopulation. The mean r_h , for all clusters, begins to increase with R_{gc} for $R_{gc} \geq 6$ kpc. As expected, we do not observe any particular trend for ellipticity or position angle, the distribution of these two parameters seems to be random. In the CMD we derive we clearly observe the two well established subpopulations of clusters in M87. We also notice the existence of a “bridge” between metal-rich and metal-poor clusters that, if actually occurring, marks the presence of intermediate metallicity clusters.

A new, but very tentative, finding of this work is that the effective radius of these old globular clusters may depend on bandpass, appearing slightly larger at bluer wavelengths. This effect is just on the margin of being statistically significant, but if it is physically real, it may point to the effects of mass seg-

regation within the clusters. Future studies from other, perhaps more nearby, galaxies should be able to test this idea more strongly.

The measurement of structural parameters of globular clusters belonging to galaxies of different Hubble type and located in different environments should reveal in the future any existent correlation between galaxy type and cluster sizes (Gómez et al. 2006). For instance, the influence of the tidal field of the host galaxy on the structural parameters of globular clusters is currently a subject of debate. Some authors believe that internal dynamics, notably two body relaxation dominate the evolution of cluster size (McLaughlin & Fall 2008). On the contrary, Gieles & Baumgardt (2008) postulate that the role of the tidal field in which a cluster is embedded is crucial in determining the cluster size. This observing program (GO 10543) has several exposures with pointings off the center of M87 (see Appendix A for details) these exposures can build a flanking field that should allow to explore further the relation between r_h and galactocentric radius. With a flanking field for M87 a new “off-center” GCLF can be build and the differences in the turnover magnitude as a function of galactocentric distance can be tested. The importance of the tidal field of the parent galaxy on the destruction of clusters can be thus explored (Ashman & Zepf 1998).

Comparing our measurements with the values derived by other teams working on this unique dataset seems a natural future step. Peng et al. (2009) reduced the data using the same procedure that we use but built the PSF using a different technique, namely the PSFs derived by Anderson and King (2006). Also, Peng et al. (2009) measured the structural parameters using KINGPHOT.

Comparing the results of KINGPHOT and ISHAPE for the same dataset can be a useful test to the strengths and deficiencies of these two codes.

Different subsets of the 2000 clusters we study deserve particular attention. One of these subsets are the clusters with larger radii. Faint fuzzy star clusters have been detected in several galaxies (Larsen & Brodie 2000, Lee et al. 2005 and references therein) and might constitute a third population of globular clusters. These so-called “fuzzies” are larger ($> 7\text{pc}$) and redder, thus more metal-rich than most clusters. Our measurements should allow us to find faint extended clusters in M87, if they exist.

Several clusters in our study have photometry in the near and far ultraviolet with HST (Sohn et al. 2006). It would be interesting to examine the optical colors and structural parameters that we derived for these subset of clusters with an UV detection. The subset of M87 clusters detected in the UV have different colors than the MW clusters leading Sohn et al. to believe that the underlying stellar population is different. These authors postulate that M87 clusters have larger populations of hot horizontal branch stars than their MW counterparts. Note that Sohn et al. (2006) found several UV sources that do not have an optical counterpart in the shallower data analyzed by Kundu et al. (1999), these sources might now be detected clusters in our dataset.

The size distribution of clusters, just like the globular cluster luminosity function, can be used as a distance indicator. It seems that the r_h size distribution is identical from galaxy to galaxy, see findings of Section 4. M87 and this particular dataset and results offers the possibility of establishing a distance based on the cluster size distribution and compare it with values ob-

tained using other methods such as the GCLF, surface brightness fluctuations, or the novae maximum magnitude rate of decline relation.

A test to the authenticity of the bridge between the two subpopulations of metal-poor and metal-rich clusters can be carried out using a Monte Carlo simulation based on the colors and luminosity function that we obtain. Such a test would constrain the scatter of our measurements and confirm or refute the physical reality of this intermediate population.

As it is the case for one-third of HST observing programs the dataset acquired under GO 10543 has been analyzed with a completely different objective than the original science goal set by the original investigators. As shown in Figure 7.1 this dataset contains a number of transient sources, as bright as globular clusters, of unknown origin. The study of this transients, probably lensing events, was the science motivation to execute this observing program.

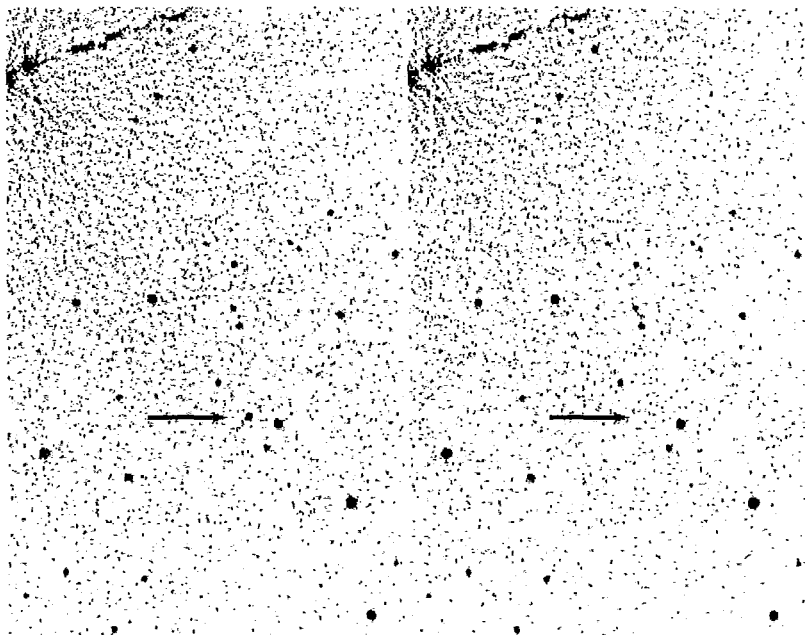


Figure 7.1 Two images at different epochs (29 Dec 2005 and 14 Jan 2006) showing a transient source as bright as nearby globular clusters. This transient is probably a nova.

Bibliography

- Aarseth, S. J. & Heggie, D. C. 1998, *MNRAS*, 297, 794
- Anderson, J., King I. R. 2006, ACS Instrument Science Report 2006-01, Baltimore, STScI
- Ashman, K. M. & Zepf, S. E. 1992, *ApJ*, 384, 50
- Ashman, K. M. & Zepf, S. E. 1998, *Globular Cluster Systems*, Cambridge University Press
- Baltz, E. A. et al. 2004, *ApJ*, 610, 691
- Baum, W. A. 1955, *PASP*, 67, 328
- Bertin, E., & Arnouts, S. 1996, *A&AS*, 117, 393
- Blakeslee, J. P., Anderson, K. R., Meurer, G. R., Benítez, N. & Magee, D. 2003, An Automatic Image Reduction Pipeline for the Advanced Camera for Surveys, ADASS XII, ASP Conference Series, Vol 295
- Blakeslee, J. P. et al. 2009, *ApJ*, 694, 556
- Brodie, J. P., & Strader, J. 2006, *ARA&A*, 44, 193
- Côté et al. 2001, *ApJ*, 559, 828
- Couture, J. et al. 1990, *ApJS*, 73, 671

- de Graaff, R. B., Blakeslee, J. P., Meurer, G. R., & Putman, M. E. 2007, *ApJ*, 671, 1624
- de Marchi, G., Paresce, F., Pulone, L. 2007, *ApJ*, 656, L65
- Dirsch, B. et al. 2003, *AJ*, 125, 1908
- Djorgovski, G. & Meylan, G. 1993, *ASP Conference Series 50, Structure and Dynamics of Globular Clusters*, San Francisco, 325
- Fall, S. M. & Rees, M. J. 1977, *MNRAS*, 181, 37
- Fall, S. M. & Rees, M. J. 1985, *ApJ*, 298, 18
- Georgiev, I.Y., Goudfrooij, P., Puzia, T.H., & Hilker, M. 2008, *AJ*, 135, 1858
- Gieles, M. & Baumgardt, H. 2008, *MNRAS*, 389, L28
- Gómez, M. et al. 2006, *A&A*, 447, 877
- Gómez, M. & Woodley, K. A. 2007, *ApJL*, 670, L105
- Gonzaga, S. et al. 2005, *ACS Instrument Handbook*, version 6.0, Baltimore, STScI
- Harris, W. E. 1996, *AJ*, 112, 1487
- Harris, W. E. 2009, *ApJ*, in press arXiv:0904.4208
- Harris, W. E. 2001, in *Star Clusters*, Saas-Fee Advanced Course 28 (New York: Springer) ed. L. Labhardt & B. Binggeli
- Harris, W. E., et al. 1998, *AJ*, 115, 1801

Harris, W. E. & van den Bergh, S. 1981, AJ, 86, 1627

Hesser, J. E., Harris, H. C., van den Bergh, & Harris, G. L. H. 1984, ApJ, 276,
491

Hodge, P. W. 1960, ApJ, 131, 351

Hodge, P. W. 1962, PASP, 74, 248

Hurley, J.R. et al. 2008, AJ, 135, 2129

Jordán, A. 2004, ApJ, 613, L117

Jordán, A. et al. 2007, ApJS, 171, 101

King, I. R. 1962, AJ, 67, 471

King, I. R. 1966, AJ, 71, 64

Kundu, A., & Whitmore, B. C., 1998, AJ, 116, 2841

Kundu, A., Whitmore, B. C., Sparks, W. B., Macchetto, F. D., Zepf, S. E., &
Ashman, K. M. 1999, ApJ, 513, 733

Kundu, A. 2008, AJ, 136, 1013

Larsen, S. S. 1999, A&AS, 139, 393

Larsen, S. S. 2008, An Ishape User's Guide

Larsen, S. S., Brodie, J. P. 2000, AJ, 120, 2938

Larsen, S. S., Brodie, J. P., Huchra, J. P., Forbes, D. A., & Grillmar, C. J.
2001, AJ, 121, 2974

- Lee, M. G., Chandar, R., & Whitmore, B. C. 2005, AJ, 130, 21218
- Mack, J. et al. 2003, ACS Data Handbook, Version 2.0, Baltimore, STScI
- McLaughlin, D. E. 1999, AJ, 117,2398
- McLaughlin, D. E., Harris, W. E., & Hanes, D. A. 1994, ApJ, 422, 486
- McLaughlin, D. E. & Fall, S. M. 2008, ApJ, 679, 1272
- Peng, E. W. et al. 2006, ApJ, 639, 95
- Peng, E. W. et al. 2008, ApJ, 681, 197
- Peng, E. W. et al. 2009, ApJ accepted, arXiv:0907.2524
- Puzia, T. H., Kissler-Patig, M., Brodie, J. P., & Huchra, J. P. 1999, AJ, 118, 2734
- Richtler, T. & Larsen, S. 2008, Globular Clusters Guides to Galaxies, Proceedings of the Joint ESO-FONDAP Workshop on Globular Clusters Held in Concepción, Chile, 6-10 March 2006
- Sirianni, M. et al. 2005, PASP, 117, 1049
- Sirianni, M., Gilliland, R., & Sembach, K. 2006 Technical Instrument Report ACS 2006-02, Baltimore, STScI
- Sohn, S. T. et al. 2006, AJ, 131, 866
- Sparks, W. et al. 1993, ApJ, 413, 531
- Spitler, L.R., Larsen, S.S., Strader, J., Brodie, J.P., Forbes, D.A., & Beasley, M.A. 2006, AJ, 132, 1593

Spitzer, L., & Thuan, T. X. 1972, ApJ, 175, 31

Strader, J. et al. 2006, AJ, 132, 2333

Tamura, N., et al. 2006a, MNRAS, 373, 588

Tamura, N., et al. 2006b, MNRAS, 373, 601

van den Bergh, S., Morbey, C., & Pazder, J. 1991, ApJ, 375, 594

Waters, C. Z., Zepf, S. E., Lauer, T. R., & Baltz, E. A. 2009, ApJ, 693, 463

West, M. J., Côté, P., Marzke, R. O., Jordán, A. 2004, Nature, 427, 31

Whitmore, B. C. 1997, Globular Clusters as Distance Indicators in The Extragalactic Distance Scale, ed. Livio, M., Donahue, M. & Panagia, N., Cambridge University Press

Wright, E. L. 2006, PASP, 118, 1711

Appendix A

The table below lists program 10543 exposures with anomalies.

Table 7.1: List of exposures with anomalies

Exposure ID	Observation Date	Comments
F606W		
j9e008orq	2006-01-12	off-center field
j9e011uaq	2006-01-14	band across field
j9e013ceq	2006-01-16	blank exposure
j9e016m9q	2006-01-19	off-center field
j9e026vxq	2006-01-29	blank exposure
j9e032pxq	2006-02-04	off-center field
j9e034w9q	2006-02-05	off-center field
j9e041rwq	2006-02-11	off-center field
F814W		
j9e008olq	2006-01-12	blank exposure
j9e008onq	2006-01-12	blank exposure
j9e008opq	2006-01-12	blank exposure
j9e016m2q	2006-01-19	blank exposure
j9e016m3q	2006-01-19	blank exposure
j9e016m5q	2006-01-19	off-center field
j9e016m7q	2006-01-19	off-center field
j9e026vqq	2006-01-29	blank exposure
j9e026vrq	2006-01-29	blank exposure
j9e026vtq	2006-01-29	blank exposure
j9e026vvq	2006-01-29	blank exposure
j9e032pqq	2006-02-04	blank exposure
j9e032prq	2006-02-04	blank exposure
j9e032ptq	2006-02-04	off-center field
j9e032pvq	2006-02-04	off-center field
j9e034w2q	2006-02-05	blank exposure

Exposure ID	Observation Date	Comments
j9e034w3q	2006-02-05	blank exposure
j9e034w5q	2006-02-05	off-center field
j9e034w7q	2006-02-05	off-center field
j9e041rpq	2006-02-11	blank exposure
j9e041rqq	2006-02-11	blank exposure
j9e041rsq	2006-02-11	blank exposure
j9e041ruq	2006-02-11	off-center field
j9e045j2q	2006-02-15	blank exposure
j9e045j4q	2006-02-15	blank exposure
j9e046mhq	2006-02-15	blank exposure
j9e046miq	2006-02-15	blank exposure
j9e046mkq	2006-02-15	blank exposure
j9e046mmq	2006-02-15	blank exposure
j9e048fsq	2006-02-21	blank exposure
j9e048ftq	2006-02-21	off-center field
j9e048fvq	2006-02-21	off-center field
j9e048fxq	2006-02-21	off-center field
j9e068qqq	2006-02-17	blank exposure
j9e068qrq	2006-02-17	off-center field
j9e068qtq	2006-02-17	off-center field
j9e068qvq	2006-02-17	off-center field
j9e094gbq	2006-02-21	blank exposure
j9e094gcq	2006-02-21	blank exposure
j9e094geq	2006-02-21	blank exposure
j9e094ggq	2006-02-21	blank exposure
j9e0a5dnq	2006-02-28	blank exposure
j9e0a5dpq	2006-02-28	blank exposure

Appendix B

In this appendix we tabulate the positions of all clusters in the final ACS/WFC image, their effective radius in each band, the average affective radius in parsecs, the flux correction used during the aperture correction, and the final magnitudes in F606W and F814W. This table contains 1822 rows, we present the first two pages in this appendix, an electronic version of this table exists.

Table 7.2: Position, effective radius, flux correction and magnitudes

X	Y	r_{hF606W}	r_{hF814W}	Average r_h	Flux correction	m_{F606W}	m_{F814W}
3193.130	42.912	3.149	3.440	3.294	1.098	23.539	22.910
4368.619	58.849	3.232	3.647	3.440	1.110	23.152	22.486
4602.950	63.972	1.823	2.528	2.176	1.014	24.193	23.373
4389.090	72.805	3.232	3.315	3.274	1.096	22.947	22.160
4459.719	73.441	1.658	2.321	1.989	1.014	24.426	23.731
4719.557	74.782	4.558	4.434	4.496	1.190	22.154	21.375
2815.065	80.420	2.611	2.652	2.631	1.029	23.784	23.189
5088.173	83.865	3.191	2.942	3.067	1.074	23.234	22.598
5414.034	91.040	2.984	3.398	3.191	1.087	24.255	23.666
2485.055	106.165	3.771	3.647	3.709	1.131	20.834	20.080
3075.344	106.960	2.321	2.942	2.631	1.029	23.173	22.354
3485.836	108.235	2.196	2.321	2.258	1.014	23.404	22.476
2704.577	117.309	1.782	2.362	2.072	1.014	24.191	23.405
2956.832	117.027	3.730	3.730	3.730	1.132	23.201	22.437
3368.786	129.598	3.067	3.647	3.357	1.104	21.239	20.382
4862.358	128.815	2.942	3.398	3.170	1.085	23.616	23.112
3621.476	130.330	1.948	2.569	2.258	1.014	25.220	24.526
2460.660	131.907	0.083	4.144	2.113	1.014	25.483	26.504

X	Y	r_{hF606W}	r_{hF814W}	Average r_h	Flux correction	m_{F606W}	m_{F814W}
4627.883	132.668	4.061	4.020	4.040	1.156	22.197	21.546
5713.884	145.659	2.486	2.569	2.528	1.018	24.806	24.621
2576.881	167.172	2.776	2.652	2.714	1.037	22.195	21.575
4093.479	167.909	2.113	2.196	2.155	1.014	23.395	22.526
4673.622	169.971	7.335	9.283	8.309	1.519	23.475	22.992
3469.313	172.286	1.906	2.196	2.051	1.014	24.143	23.529
2286.166	194.908	2.652	2.694	2.673	1.033	21.810	21.084
3194.419	202.969	2.569	2.569	2.569	1.022	23.597	22.956
3110.014	205.321	0.124	0.332	0.228	1.000	21.766	21.357
3655.067	217.319	4.393	5.139	4.766	1.210	22.734	21.885
4090.081	217.847	3.149	2.776	2.963	1.063	22.924	22.224
3919.925	226.865	2.155	2.776	2.466	1.013	23.908	23.038
5006.069	234.750	2.528	2.776	2.652	1.031	22.820	22.001
5247.703	235.401	4.185	4.061	4.123	1.162	24.152	23.540
2538.067	245.464	2.652	2.694	2.673	1.033	22.338	21.635
4735.007	245.258	2.611	2.735	2.673	1.033	23.327	22.806
2026.989	256.589	2.776	3.481	3.129	1.081	24.524	24.063
545.186	257.876	2.984	2.942	2.963	1.063	20.860	20.133
3889.533	260.225	2.652	2.694	2.673	1.033	22.969	22.342
3933.358	274.951	2.694	3.357	3.025	1.070	24.114	23.209
2541.536	276.079	2.611	2.901	2.756	1.042	23.838	23.311
2175.250	282.089	2.901	2.859	2.880	1.055	21.135	20.430
2871.759	281.725	2.569	2.652	2.611	1.026	21.556	20.680
3033.421	284.026	1.948	2.321	2.134	1.014	24.664	23.740
4663.983	283.552	2.238	2.321	2.279	1.014	22.710	21.790
3645.155	285.476	2.776	3.315	3.046	1.072	23.175	22.515
549.112	291.144	4.144	4.144	4.144	1.164	21.391	20.511
2564.533	300.057	3.937	4.310	4.123	1.162	24.253	23.626
3409.781	309.119	2.486	2.652	2.569	1.022	23.633	22.781
2249.199	320.162	3.232	3.232	3.232	1.092	24.094	23.563
4645.841	327.802	5.014	5.139	5.076	1.234	22.478	21.850
2564.347	329.217	2.735	2.984	2.859	1.053	22.945	22.141